ISSN 1349-1121
JAXA-RM-13-012E

JAXA Research and Development Memorandum

Overview of the JAXA Helicopter Research Activity

Shigeru SAITO, Yasutada TANABE, and Noboru KOBIKI

October 2013

Japan Aerospace Exploration Agency

Overview of the JAXA Helicopter Research Activity*1

Shigeru SAITO*, Yasutada TANABE** and Noboru KOBIKI***

Abstract

In JAXA, study of the aerodynamic performance/dynamics and aeroacoustics for helicopter has been conducted by two approaches. One is the theoretical approach using the comprehensive code such as the Local Momentum Theory/prescribed wake model and numerical simulation approach such as 3D Euler/Navier Stokes code so far. The other is experimental approach using low speed wind tunnel such as JAXA low speed wind tunnel (5.5m width x 6.5m height test section).

In the theoretical approach, the comprehensive code named LMT has applied to investigate several kinds of helicopters such as single, tandem and coaxial type helicopters. Also this is used to investigate the dynamic effect of a helicopter by atmospheric gust and tip vortex generated from a large scale jet airplane. To develop the CFD code, Euler formulation is mainly applied to investigate the flow field around a helicopter rotor, especially to capture the tip vortex generated from blade tip region. In the code, the SLAU scheme was applied to capture the more precise vortex system generated from blade root region, usually the flow speed around a root of a blade is much lower compared with the outer region of blade. The effect of elastic deformation of a blade has also been included in this code to obtain the more precise aerodynamic characteristics.

In the experimental approach, the JAXA Multi-purpose Rotor Test Stand (JMRTS) with 2m rotor diameter has been constructed to investigate the aerodynamic/aeroacoustic performance of a helicopter. The active devices such as an active flap have been installed on a rotor blade and tested to evaluate the device performance on the aerodynamics/aeroacoustics.

JAXA has conducted several kinds of helicopter research so far. For example, the study of dynamic response of helicopter which penetrates into the tip vortices generated from a large airplane such as Jumbo Jet, the study of performance of wind turbine with elastic blade, the study of the performance of Advanced Turbo Prop with single rotating propeller or counter rotating propeller, the dynamic response of helicopter in auto-rotation flight, the study of aerodynamic performance of tandem rotor in yawed flight and the study of the aerodynamic performance of coaxial rotor. Since 2008, the design of a real-sized low noise helicopter rotor blade with the JAXA developed active flap system has started in order to validate the effect of an active flap system. Within the three years, the conceptual design, the engineering study including analytical dynamic evaluation and the bench tests evaluating static, dynamic and endurance performances have been completed.

This paper described the overview of the helicopter research activities in JAXA. It includes the explanation of theoretical analysis code which has been developed for examples, Local Momentum Theory and CFD code and wind tunnel test stand. Various examples of results will be described in this paper.

Keywords: Helicopter research activity, LMT, BVI noise, CFD, Wind tunnel test stand, Control, Fire-fighting helicopter

1. INTRODUCTION

Helicopters have a great potential to operate in the normal/critical activities such as life-saving, fire-fighting, air rescue, transportation, police observation, broadcasting from the sky and so on. Japan has lots of volcanoes and disasters such as Typhoon, earthquake and Tsunami. Over 15,000 people died and over 3,000 people are still missing due to the great East Japan earthquake and Tsunami on March 11th in 2011. Over 600 helicopters from the fleet of the fire and disaster management agencies and Japan Ground Self-Defense Forces (The ministry of Defense), etc. had come together to Tohoku area for the disaster relief. In the early stage of this tragedy, helicopters played an important role to save lives and extinguish the fire and transport so many foods and daily commodities and persons. If there were not so many helicopters, it can be said that the number of people died and missing people might be huge. Thus the usefulness of helicopter for the great disaster has been proven, especially in Japan.

However helicopters have many issues to be solved as shown in Figure 1. There are two different aspects to be solved, one is the operation and the other is pure technology aspect. Figure 1 shows the technical issues for a helicopter. In these serious issues of a helicopter, the aeroacoustics is the most important issue for the wide range activities of a helicopter. Also, vibration and various kinds of interference are important issues due to the increase of aerodynamic drag, that is, the increase of the necessary power.

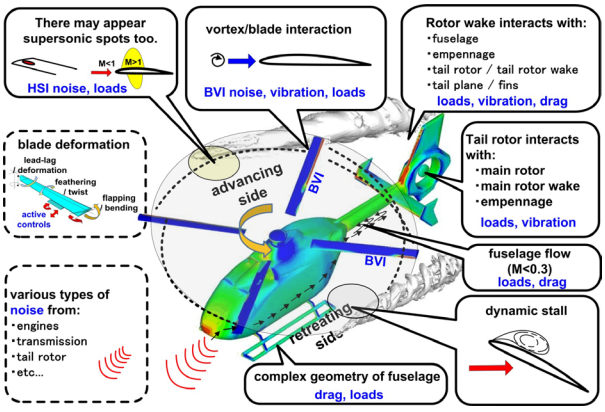

Figure 1. Issues for helicopter.

Since 1985, JAXA (formally NAL) has started the research activities on helicopter. The research activity has been conducted by means of the development of analytical codes such as Local Momentum Theory (LMT) or Local Circulation Method (LCM) at the beginning stage. Then the CFD techniques have been introduced in the analysis of the flow field around a rotor.

The rotor test stand has also been developed in order to

*1 Received 5 September 2013

Formerly, Operation and Safety Technology Team, Aviation Program Group, JAXA, Japan
* Presently Program Management and Integration Department, Institute of Aeronautical Technology, JAXA, Japan (Tel: +81-50-3362-3152, Email: ssaito@chofu.jaxa.jp)
** Presently Aircraft Systems Research Group, Institute of Aeronautical Technology, JAXA, Japan (Tel: +81-50-3362-3357, Email: tan@chofu.jaxa.jp)
*** Presently Aircraft Systems Research Group, Institute of Aeronautical Technology, JAXA, Japan (Tel: +81-50-3362-2098, Email: kobiki@chofu.jaxa.jp)

investigate the rotor performance and evaluate the noise/acoustic level and validate the capability of control to reduce the vibration and noise level of a rotor.

In this paper, the histories of the JAXA helicopter research activities which have been conducted so far are reviewed.

2. EXPERIMENTAL APPARATUS

2.1 Wind tunnel facilities in JAXA [1]

Since 1952, JAXA (formerly NAL) has restarted the R & D of Aeronautics because of the World War II. At the beginning, several kinds of wind tunnel test facility have been constructed in Chofu Aerospace Center in Figure 2. Figure 3 shows the wind tunnel facilities related with various types of vehicle and Table 1 shows the several kinds of wind tunnels and its performance in JAXA.

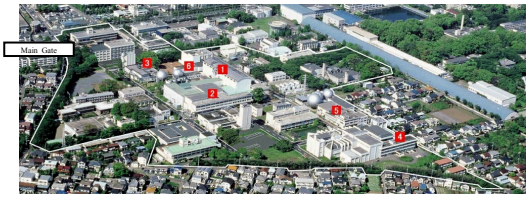

Figure 2. Chofu Aerospace Center (Administrative Office).

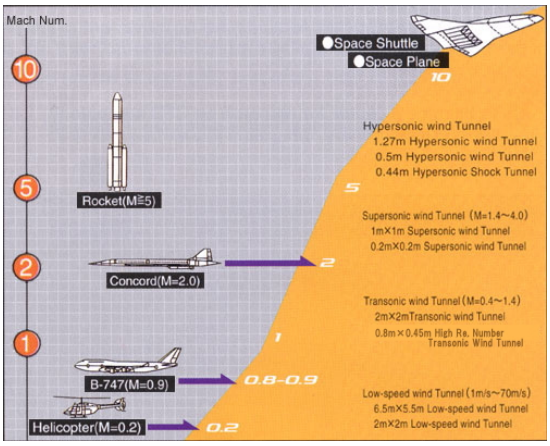

Figure 3. Various type of wind tunnel for types of vehicle.

Table 1. Wind tunnels in JAXA and its performance.

Name of wind tunnel	Velocity range	Type of operation	Year of completion
① 6.5m×5.5m Low speed wind tunnel	V=1-70m/s	Continuous, circulation type	1965
2m×2m Low speed wind tunnel	V=3-60m/s	Continuous, circulation type	1971
② 2m×2m Transonic wind tunnel	M=0.1-1.4	Continuous, circulation type	1960 1994 refinement
0.8m×0.45m High Re. Number Transonic wind tunnel	M=0.2-1.4	Intermittent, blow down	1979 1997 refinement
③ 1m×1m Supersonic wind tunnel	M=1.4-4.0	Intermittent, blow down	1961 1999 refinement
0.2m×0.2m Supersonic wind tunnel	M=1.5-2.5	Continuous, circulation type	1994
④ 0.5m Hypersonic wind tunnel	M=5,7,9,11	Intermittent, blow down + vacuum suction	1965
⑤ 1.27m Hypersonic wind tunnel	M=10	Intermittent, blow down + vacuum suction	1994
0.44m Hypersonic Shock Tunnel	M=10,12	Non-diaphragm driven impulse wind tunnel 2 stage compressed impulse wind tunnel	1967 1994 refinement
750kW ark heated wind tunnel	M=4.8	Contraction flow stability ark heated wind tunnel	1981 1993 refinement

There are four major wind tunnels in Chofu Aerospace Center of JAXA, (1) Low Speed wind tunnel (5.5m x 6.5m), (2) Transonic wind tunnel (2m x 2m), (3) Supersonic wind tunnel (1m x 1m) and (4) Hypersonic wind tunnel (0. 5mΦ and 1.25mΦ).

Figure 4 shows the schematic view of the Low Speed wind tunnel. The speed range is between 1 to 70 m/s and test section is 6.5 m in height and 5.5 m in width.

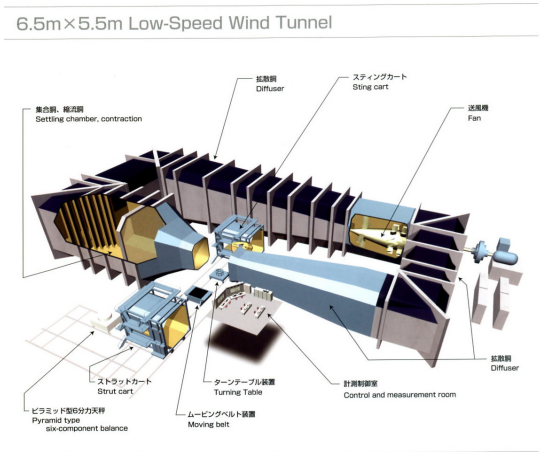

Figure 4. Schematic view of Low Speed Wind Tunnel.

Figure 5 shows the schematic view of 2 m x 2 m transonic wind tunnel. The speed range is between 0.1 to 1.4 Mach number and test section is 2 m height x 2 m width.

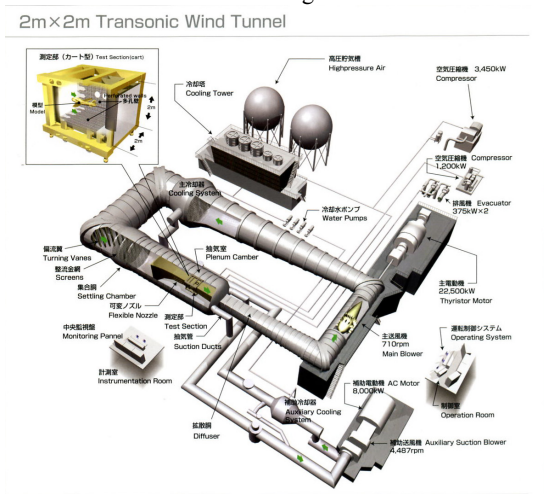

Figure 5. Schematic view of Transonic Wind Tunnel.

Figure 6 shows the schematic view of Supersonic wind tunnel. The speed range is between 1.4 to 4.0 Mach number and test section is 1 m height x 1 m width.

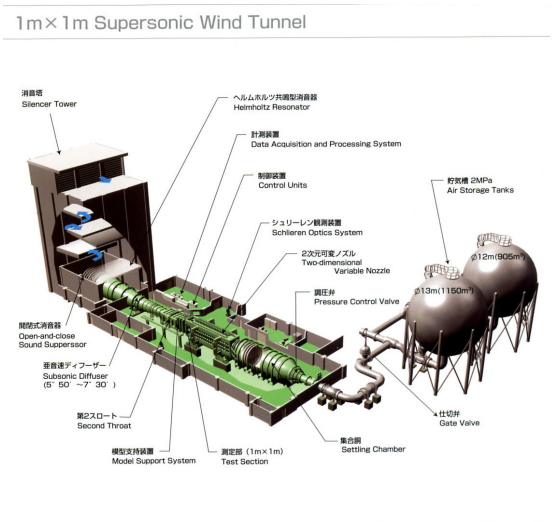

Figure 6. Schematic view of Supersonic Wind Tunnel.

Figure 7 shows the schematic view of hypersonic wind

tunnel. The speed range is between Mach number =5, 7, 9, 10, 11 and test section is 0.5 m diameter at Mach number = 5, 7, 9, 11 and 1.27 m diameter at Mach number =10.

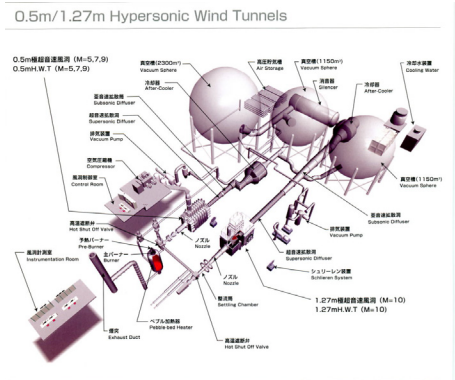

Figure 7. Schematic view of Hypersonic Wind Tunnel

On the other hand, in the Chofu airdrome base as shown in Figure 8, there are two types of wind tunnel. One is the low speed wind tunnel, which test section is 2m x 2m as in Figure 9; the other is supersonic wind tunnel, which test section is 0.2m x 0.2m as in Figure 10. These two wind tunnels are mainly used for the basic researches.

Figure 8. Chofu Aerospace Center (Airdrome base).

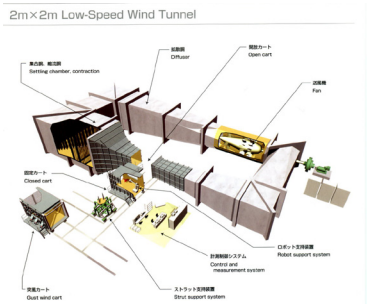

Figure 9. Schematic view of Low Speed Wind Tunnel.

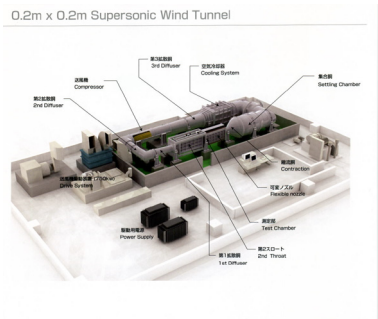

Figure10. Schematic view of Supersonic Wind Tunnel.

2.2 Rotary wing test apparatus

In JAXA, two types of rotary wing apparatus have been developed so far. One is the JAXA Multipurpose Rotor test Stand (JMRTS) [2] and the other is a one-bladed Rotor Test Stand [3].

The JMRTS have been used to investigate the aerodynamic performance and the aerodynamic interference between rotor and fuselage. Recently it has been used to measure the aeroacoustic properties such as high speed impulsive (HSI) noise and blade vortex interaction (BVI) noise. Special devices such as active flap have been used to investigate the noise reduction capabilities. Figure 11 shows the photograph of JMRTS and schematic view of control units. Table 2 shows the specification of JMRTS.

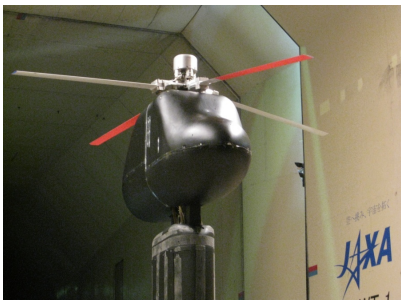

(a) Photograph of the JMRTS in Low Speed wind tunnel

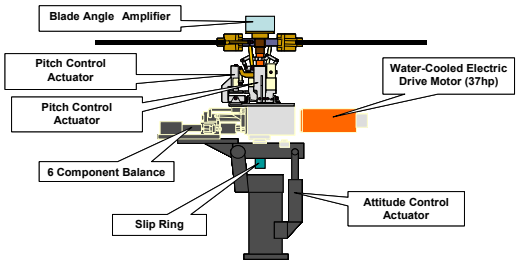

(b) Schematic view of the JMRTS components

Figure 11. Schematic view of JMRTS in JAXA LWT.

Table 2. Specification of JMRTS.

Units of JMRTS	Specification
Rotor Radius	2 m
No. of blades	4
Maximum Rotor rpm	2600 rpm
Blade pitch operation range For Collective Pitch angle For Cyclic Pitch angle	 -5° ~ 20° -10° ~ 10°
Rotor hub system	Articulated
Electric power	200V Three-phase circuit
Drive Motor	27.5KW (11500rpm) + Gear Box
Cooling system For Motor For Gear box	 Water cooling (circulation) Oil cooling (including lubrication)

The other apparatus is one-bladed rotor test stand in Figure 12. This rotor test stand has been used to investigate the performance of the new types of device such as active tab and active flap.

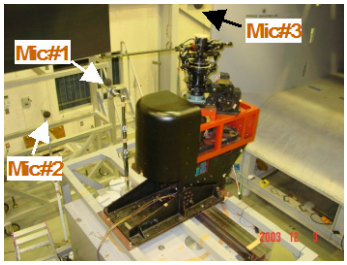

Figure 12. Schematic view of One-bladed Rotor Test Stand.

The specification of the one-bladed rotor test stand is shown in Table 3.

Table 3. Specification of one-bladed rotor test stand.

One-bladed rotor	Specification
Rotor radius	1 m
Maximum Rotor rpm	1200 rpm
Hub type	Rigid in flap and lead-lag
Blade pitch operation range For Collective Pitch angle For Cyclic Pitch angle	 -5° ~ 15° zero
Airfoil	NACA0012
Blade chord	0.12 m
Planform	Rectangular

3. WIND TUNNEL TEST

3.1 Research on helicopter noise

Figure 13 shows the various kinds of noise generated from a helicopter. In these noises, the high speed impulsive and blade vortex interaction noises are most annoying noise compared with other noise sources. The following paragraphs explain the results of the wind tunnel test for noise characteristics.

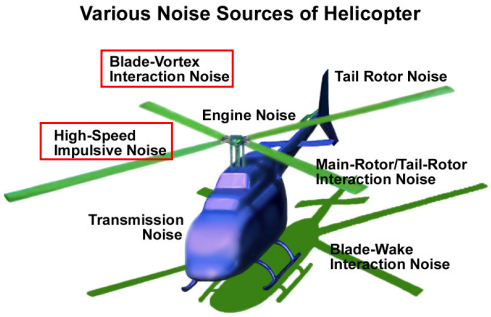

Figure13. Various noise sources from a helicopter.

(a) High Speed Impulsive (HSI) Noise [4]

The HSI noise has been measured in the Low Speed wind tunnel in 2000. The main purposes of this wind tunnel test are to check the operation capability of a new developed rotor test stand and measure the high speed impulsive noise and establish the database of HSI noise. Figure 14 shows a photograph of the JMRTS setting in the Low Speed wind tunnel.

Figure 14. JMRTS setting in Low Speed wind tunnel.

When the rotor rotational speed become very high, HSI noise is generated from a rotor, in this test case, the rotor rotational speed was 2400 rpm and tip Mach number was 0.898. For the prevention of an accident, the acoustic materials were used around the JMRTS and it was also used to prevent the blade splash as shown in Figure 15 and 16.

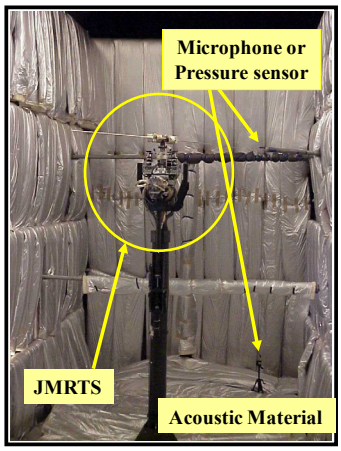

Figure 15. JMRTS setting and noise measurement system

Figure 16. Microphone setting in Low Speed wind tunnel

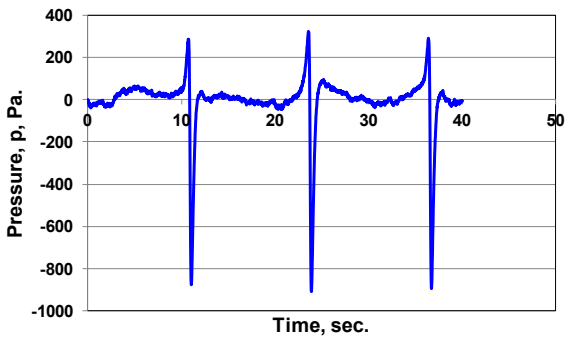

Figure 17. Example of the HSI noise measured (Mtip=0.898 , position=1.1R from the center of rotor)

(b) Blade Vortex Interaction (BVI) Noise [5,6]

In the descending regime or approach to the landing area for a helicopter, the Blade Vortex Interaction (BVI) noise is usually generated. The noise is caused by the collision of the tip vortices with the preceding or present blade. Once this noise is generated, the noise level becomes very high and very spiky sound is generated depending on the number of blades. To measure and establish a database of BVI noise, wind tunnel test has been conducted in the JAXA Low Speed wind tunnel in collaborating with MHI. Figure 18 show the photograph of the JMRTS in JAXA Low Speed wind tunnel. The surface of this apparatus was covered with sound proof material. Three microphones were installed inside of the test section of wind tunnel.

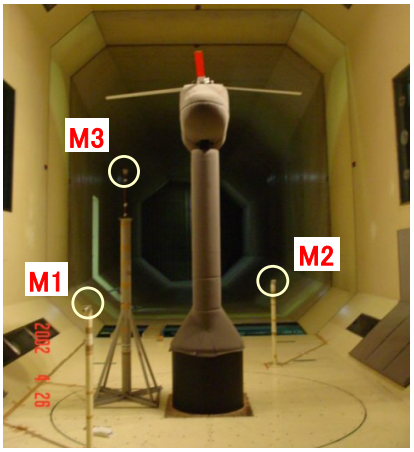

Figure 18. JMRTS setting in Low Speed wind tunnel.

Figure 19 shows an example of results from this wind tunnel test. It shows the BVI noise level against advanced ratio. From these figures, it is clearly shown that the maximum values of the BVI noise exist near the advance ratio of 0.15. As the shaft angle becomes large, the advance ratio decreases. Figure 20 shows the typical waveform of the BVI noise at the observer's position. In this case, the data in 30 revolutions are used in order to get the ensemble average data. In this wind tunnel test, rotor has four blades, that is why the BVI noises are observed four times in one rotor revolution shown in this figure.

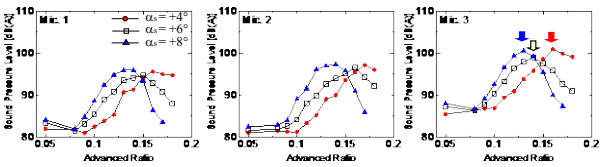

Mic. 1 (Front Position) Mic. 2 (Rear Position) Mic. 3 (Side Position)

Figure 19. BVI Noise level at each microphone position.

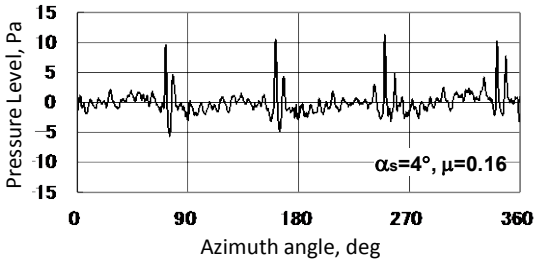

Figure 20 Waveform of BVI noise at Mic.3. (C_T=0.008, 1000 rpm)

3.2 Researches on active devices

(a) Active Tab [7~10]

Recently new concepts in order to reduce or alleviate the noise level have been introduced for helicopter blade. One of the candidates is an active tab which is installed at the trailing edge near blade tip region. The mechanism to drive an active tab is to push and pull the tab from the trailing edge. As the active tab increases the surface area, the local lift on a blade increases and the aerodynamic pitching moment to twist a blade generates on a blade. As a result, the torsional deflection might be occurred on the blade. This elastic deformation will change the released direction of tip vortex generated from the blade tip. This is the fundamental mechanism to reduce the rotor aerodynamic noise.

In JAXA, active tab has been introduced in order to reduce the rotor aerodynamic noise such as BVI noise. Figure 21 shows the rectangular blade installed with an active tab. In this case, the displacement of tab is set to be 24 mm (Rotor radius is 1 m) and anhedral angle of tab is 10 degrees shown in this figure. To evaluate the capability of noise reduction of an active tab the wind tunnel test has been conducted using one-bladed rotor test stand.

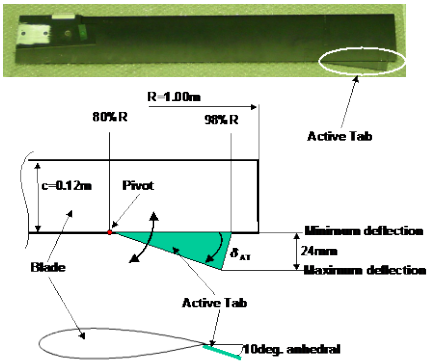

Figure21. Blade with active tab and its design features.

The main purpose of the usage of an active tab is to reduce the BVI noise generated from a rotor. To realize this concept, the following control system is constructed as shown in figure 22. In this control system, pressure change on a blade surface by BVI phenomenon was used as an index of noise level instead of the noise observed by microphone. The optimal control theory has been used to get the optimal solution of blade pitch angle to reduce the BVI noise. Data in 40 revolutions were used to get the ensemble average of measurement values. After the every 40 revolution, the optimal control inputs have been calculated by using this optimal control theory.

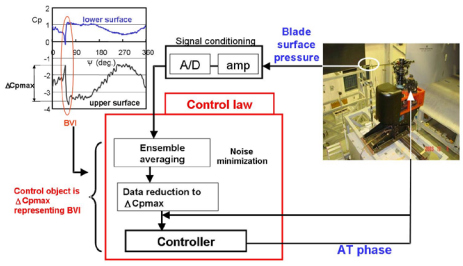

Figure 22: Control system in wind tunnel testing.

Figure 23 shows typical results of the wind tunnel test. Compared with no control case, this controller works well and showed 2dB noise reduction capability and about 3 dB noise controllability.

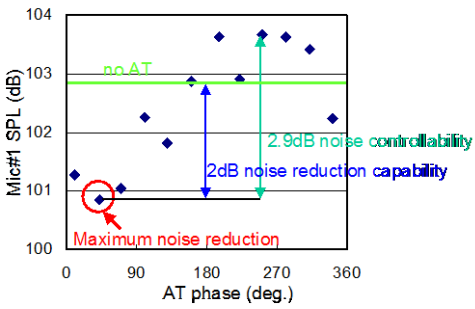

Figure 23. Noise reduction capability by an active tab.

(b) Active Flap [11~13]

Following to the active tab, the capabilities of an active flap has been evaluated using same test stand. A blade installed an active flap at the trailing edge near the blade tip shown in the figure 24.

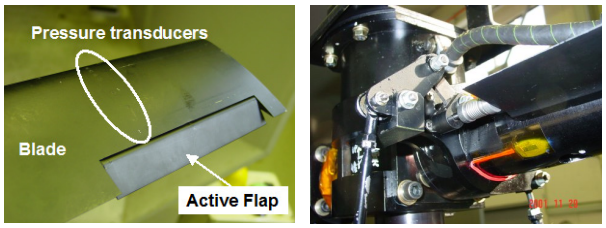

Figure 24. Blade with an active flap and manipulation mechanism.

Same control has been used in this active flap case to reduce the BVI noise, which is shown in figure 25. The two results by this control have been shown in this figure. From this figure, it is shown that the minimum noise reduction was appeared at the specific phase angle of an active flap system. Around the 120 degrees of phase angle the minimum sound pressure level (SPL) was shown in the left figure of figure 25. On the other hand, this control converged to the target SPL value as shown in the right figure of figure 25. Figure 26 shows the capability of noise reduction of this control. The left figure shows the case of without control case. The middle and right figures show the results of control case. The middle figure shows the minimum noise case, the right result shows the maximum noise case. Sound pressure level depended on the phase angle of the active flap activation. Almost half reduction of sound pressure level has been performed by this system as shown in this figure.

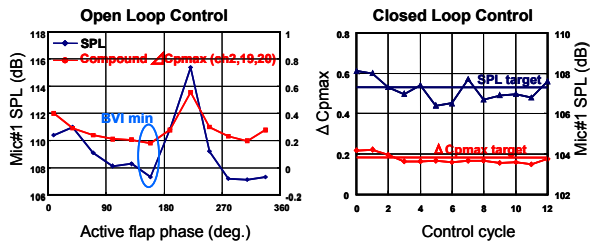

Figure 25. Wind tunnel test result of closed loop control with compound ΔCpmax

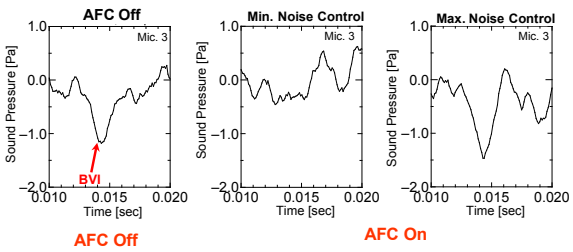

Figure 26. Time history of sound pressure on the blade Surface . (Wind Speed= 25 m/sec, N= 600rpm)

The specific wind tunnel such as anechoic wind tunnel should be needed in order to investigate of the precise understanding of the BVI phenomena. Also, the precise investigation about the control should be done by both theoretical analysis and wind tunnel test.

3.3 Research on Rotor-Fuselage interaction [14~17]

The aerodynamic interference between rotor and fuselage is very important for the helicopter performance, especially rotor torque (engine power), noise, and vibration and so on. In view of the BVI noise reduction, the wind tunnel test to investigate the interference between rotor and fuselage using JMRTS with fuselage has been conducted in 2008 in JAXA Low Speed wind tunnel. To investigate the interference between rotor wake and fuselage, pressure sensors have been embedded on the surface of the fuselage as shown in figure 27. Figure 28 shows the rotor performance with regard to rotor rotational speed. For each rotational speed, the rotor performance has been shown the almost same aerodynamic property.

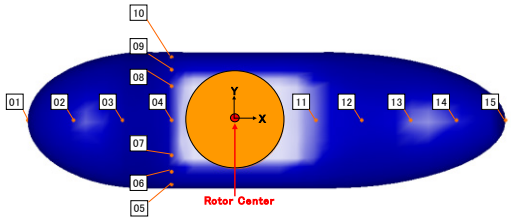

Figure 27. Pressure sensors embedded on the fuselage surface

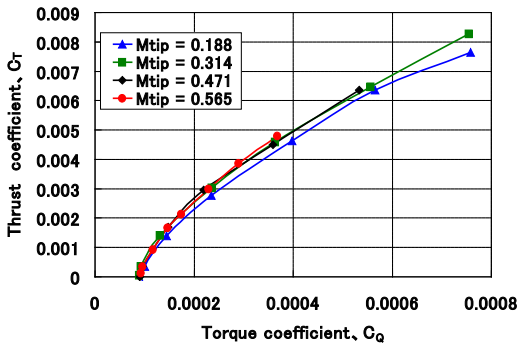

Figure 28. Rotor polar curve with regard to tip Mach number

Figure 29 shows the pressure fluctuation at the sensors positions of the cross section on the fuselage surface. In this figure, the pressure fluctuation depends on the position of the sensor installed on the fuselage surface. As rotor rotates, the peak position of the pressure fluctuation moves in the rotating direction. Just beneath of rotor, the fluctuation of pressure shows the most severe. The pressure fluctuations along the center line on the fuselage are shown in figure 30. In this figure, the pressure distribution rear body is very distinctive due to the flow separation and the generation of extra vortices etc.

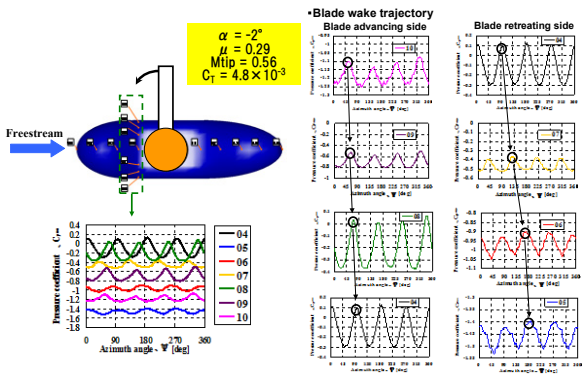

Figure 29. Pressure fluctuation of the sensors located on the cross line of the fuselage.

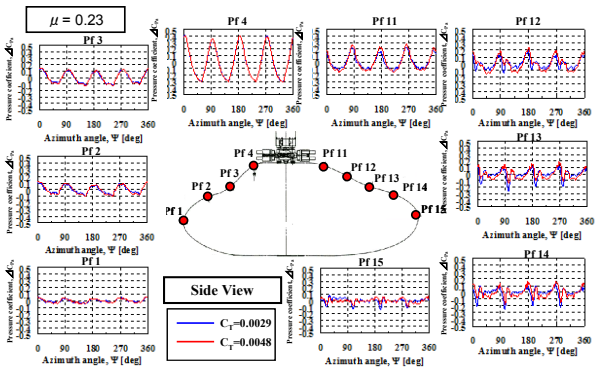

Figure 30. Pressure fluctuation of the sensors along the center line of the fuselage.

Figure 31 shows the comparison of the CFD calculation results using rFlow3D with the experimental data. (a) and (b) in figure 31 show data of the pressure distribution across the fuselage and those along the center line of fuselage. CFD calculation shows the good correlation with experimental data.

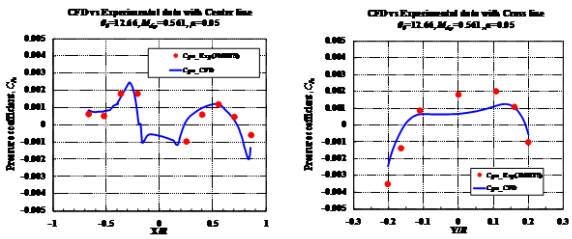

(a) Center-line (b) Cross-line

Figure 31. Comparison of pressure distribution of fuselage between CFD calculation results and experiment data.

4. NUMERICAL ANALYSIS TOOLS

There are several analytical tools which could evaluate the aerodynamic performance and simulate the dynamics of rotors. Momentum Theory is the typical tool to estimate the rotor aerodynamic performance; however it could not simulate the individual behavior of blade. Blade Element Theory (BET) is the very useful tool to analyze the rotor performance. The each section on a blade is treated as 2D airfoil. As a result, rotor aerodynamic performances such as thrust, torque, pitching and rolling moment are calculated by integrating for each section. The accuracy of this simulation depends on the accuracy of estimation of induced velocity. Vortex theory has good potential to estimate the aerodynamic performance of a rotor, especially free wake vortex theory shows more precise estimation of a rotor performance. BET can be used even in the vortex theory. The combination between BET and momentum theory, vortex theory (even prescribed wake or free wake, etc) can be easily applied to simulate the blade dynamic behavior, for example blade dynamic behavior by deformation and atmospheric disturbance.

Professor A. Azuma and his colleagues in his laboratory have developed the aerodynamic analytical tools for helicopter in the 1970's [18,19]. These tools are based on the combination of momentum theory and blade element theory. Compared with other aerodynamic tools such as vortex theory, this tool needs more short computing time to calculate the rotor aerodynamic and dynamic properties of helicopters.

On the other hand, to obtain the more detail information of the flow field around a rotor or fuselage, CFD technique might be most useful tool. In JAXA, the CFD code using Euler equations has been developed so far. This code has been applied to various aerodynamic phenomena of a helicopter.

The following sections describes in more detail about these analytical tools.

4.1 Local Momentum Theory

In the Local Momentum Theory (LMT), the induced velocities at each blade spanwise position have been determined by means of the instantaneous momentum balance at specified spanwise position. The basic theory is described below. First of all, an elliptical wing has an elliptical lift distribution as shown in figure 32. The induced velocity distributed on the elliptical wing is constant as v_0. This value is half compared with the velocity at the infinite distance. It is supposed that the arbitrary wing is decomposed by the N elliptical wings (Fig.33). In this figure, (a) shows the symmetrical arrangement and (b) shows the one-sided arrangement. Supposed that the lift is L_i and constant induced velocity is Δv of the *i*-th wing, then total lift of this wing become as follows.

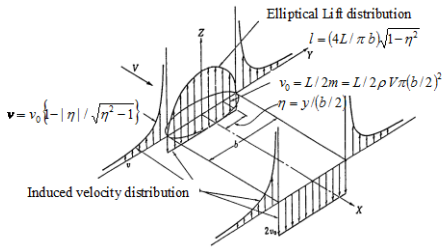

Figure 32. Airloading and induced velocity distribution of an elliptical wing.

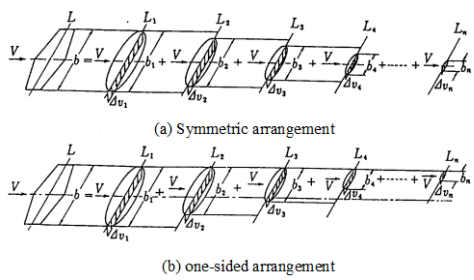

Figure 33. Decomposition a straight wing to an elliptical wing.

$$L = \sum_{i=1}^{N} L_i = \sum_{i=1}^{N} 2\rho\pi(b_i/2)^2 V\Delta v_i \qquad (4\text{-}1\text{-}1)$$

Let think about the symmetrical arrangement of an arbitrary wing. If the upwash of the *i*-th elliptical wing can be ignored, then a lift and an induced velocity can be obtained at the arbitrary elliptical wing as follows respectively.

$$l_j = \sum_{i=1}^{j} l_i(\xi) = \sum_{i=1}^{j} (4L_i/\pi b_i)\sqrt{1-\xi^2} \qquad (4\text{-}1\text{-}2)$$

$$v_j = \sum_{i=1}^{j} \Delta v_i$$

Where $\xi = y/(b_i/2) = \eta(b/b_i)$, b is span length of an arbitrary

wing. To determine the induced velocity, Δv_j, of the j-th elliptical wing, the lift at the local position $(-\eta_i, -\eta_{i-1})$ has to balance between the lift generated by the blade element theory and the lift by local momentum as follows.

$$l_i = \int_{-\eta_j}^{-\eta_{j+1}} (1/2)\rho V^2 c_j a \left\{ \theta_j - \sum_{i=1}^{j} (\Delta v_i / V) \right\} (d\eta / \Delta\eta_j) \tag{4-1-3}$$

$$= \sum_{i=1}^{j} 2\overline{m_i} \Delta v_i$$

where,

$$\Delta\eta_j = \eta_j - \eta_{J+1}$$

$$\overline{m_i} = \int_{-\eta_j}^{-\eta_{j+1}} \rho b_i V \sqrt{1-(b/b_i)^2 \eta^2}\, (d\eta / \Delta\eta_j)$$

$$c_j = c\left[1-(\eta_j + \eta_{j+1})/2\right]$$

$$\theta_j = \theta\left[1-(\eta_j + \eta_{j+1})/2\right] \tag{4-1-4}$$

$c_j, \theta_j, \overline{m_i}$ are the chord, pitch angle, mass of the flow passing through the circle with the diameter based on the span length of the i-th wing of the j-th ellipsoidal wing, ρ, a are air density and 2D lift slope of the wing section. The j-th induced velocity of the j-th elliptical wing, can be obtained in the Eq. (4-1-2). In the case of the one-sided arrangement, the same procedure can be applied in order to obtain the induced velocity.

To apply this method to the rotary wing, a rotating blade is decomposed in to N elliptical wings as shown in figure 32. (Strictly speaking, as a rotating blade is operating in the shear flow, the wing having elliptical lift distribution does not have elliptical wing shape. However the elliptical wing shape is supposed in this method.).

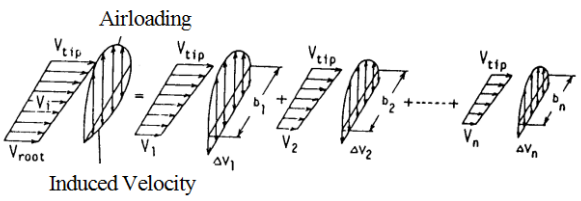

Figure 34. Decomposition of a rotary wing to wings having elliptical circulation distribution.

Each decomposed elliptical wing is distributed in the one-sided arrangement. In the arrangement, the mass passing through the i-th elliptical wing at the position of (x_i, R, R) is obtained in the following equation.

$$m_i = \rho S_i V_{i,c}$$

$$= \rho\pi \{R(1-x_i)/2\}^2 \{V \sin\varphi + R\Omega(1+x_i)/2\} \tag{4-1-5}$$

where,

$$x = \{(1+x_i) + \xi(1-x_i)\}/2$$

or

$$\xi = \{2x - (1+x_i)\}/(1-x_i)$$

At x span position, lift can be obtained with the same way of fixed wing case as follows.

$$l_i = \int_{x_i}^{x_{i+1}} (1/2)\rho V_i^2 c_i a(\theta_i - \phi_i)(dx/\Delta x_i)$$

$$= \int_{x_i}^{x_{i+1}} \sum_{i'}^{i} [4L_{i'} / \{\pi R(1-x_i)\}]$$

$$\times \left[\left\{ R\Omega x + V \sin\left(\varphi_{k,0} + \sum_{\lambda=1}^{j-1} \Delta\varphi_\lambda \right) \right\} \right] \tag{4-1-6}$$

$$\times \sqrt{1 - \{(2x - 1 - x_{i'})/(1-x_{i'})\}^2}\, (dx/\Delta x_i)$$

where,

$$\Delta x_i = x_{i+1} - x_i$$

$$V_i = V \sin\left(\varphi_{k,0} + \sum_{\lambda=1}^{j-1} \Delta\varphi_\lambda \right) + R\Omega\{(x_i + x_{i+1})/2\}$$

$$c_i = c[x = (x_i + x_{i+1})/2]$$

$$\theta_i = \theta[x = (x_i + x_{i+1})/2] \tag{4-1-7}$$

$$\phi_i = (V_N + v_{l,m} + v_{i,j,k})/V_i$$

$$V_N = V \sin(i_s)$$

$$L_i = 2\rho S_i V_{i,c} (v_{i,j,k} - v_{i-1,j,k})$$

where $\varphi_{k,0}$ and $\Delta\varphi$ are the initial value of the azimuth angle and step value for the k-th blade. Horizontal speed V_i, θ_i and ϕ_i are function of azimuth angle, therefore each parameter has subscript of j and k. However in the above equation, such subscript is omitted for abbreviation. Subscript if i, j and k means the spanwise position, time or azimuth angle and k-th blade respectively. Once the induced velocity can be obtained using above procedure, a lift distribution along a blade span can be obtained. However the helicopter blade encounters the induced velocity generated by a preceding blade. To realize the phenomena, the mesh is introduced in the calculation as shown in figure 35. At the local mesh (l', m'), the induced velocity for each blade remains at every time step. This process is explained in figure 34.

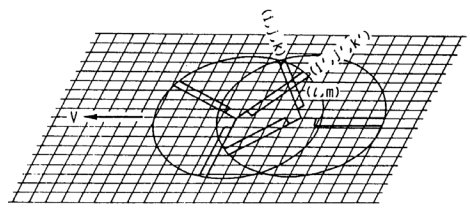

Figure 35. Representation of the successive impulse of a local station in the rotor plane of an advancing rotor.

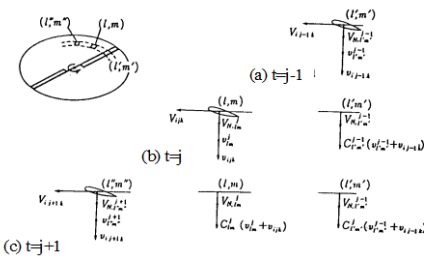

Figure 36. Successive change of the induced velocity in the rotational plane of a rotor.

At $t = j-1$, let suppose that a blade element proceeds with speed $V_{i,j,k}$. The vertical velocity has three components as vertical component of forward speed, V_N, induced velocity generated by the blade itself, $V_{i,j-1,k}$ and resultant induced velocity generated by preceding and own blade, $v_{l',m'}^{j-1}$. At mesh positions (l,m) and (l'',m''), at which a blade pass through at time $t=t$ and $t=t+1$ respectively, induced velocity still remains. However the magnitude of induced velocity maintains no more the same values. The attenuation coefficient, C, will introduce in order to estimate the decay rate of the induced velocity as shown in figure 36. This coefficient, C, is the function of span position, azimuth angle, namely time. At time, $t = j$, the induced velocity is defined as

$$v_{lm}^{j} = C_{lm}^{j-1}\left(v_{lm}^{j-1} + \sum_{i=1}^{N}\sum_{k=1}^{B} v_{i,j-1,k}\,\delta_{lm}\right) \tag{4-1-8}$$

where B is the number of blades. The definition of this attenuation coefficient is explained in ref .[18,19] in detail.

The LMT was applied to the windmill aerodynamics with some modification. This new method is referred to as "Local circulation method (LCM). The main modification is described as follows. Each blade element is expressed by the bound vortex and induced velocity at 25% chordwise position is decided by assumption that local flow at 75% chordwise position pass through along the wing. This method is described in ref.[20].

These two analytical tools were applied to the various phenomena in order to investigate the aerodynamic properties of the helicopter rotors and windmill, propeller, advanced turbo prop propeller etc.

4.2 rFlow3D [21]

4.2.1 Governing equations

The flow solver used to compute the flow field is based on the Euler equations discretized with the finite volume method. Because the rotor blade is moving and deforming, an Arbitrary Lagrangian-Eulerian (ALE) formulation [22] is used. The governing equations are

$$\frac{\partial}{\partial t}\int_{V(t)} \mathbf{U}dV + \int_{S(t)} \mathbf{F}\cdot\mathbf{n}dS = 0 \tag{4-2-1}$$

where,

$$\mathbf{U} = \begin{pmatrix} \rho \\ \rho\mathbf{v} \\ \rho e \end{pmatrix} \tag{4-2-2}$$

is the conservative variables vector and

$$\mathbf{F} = \begin{pmatrix} (\mathbf{v}-\dot{\mathbf{x}})\cdot\mathbf{n}\rho \\ (\mathbf{v}-\dot{\mathbf{x}})\cdot\mathbf{n}\rho\mathbf{v} + p\mathbf{n} \\ (\mathbf{v}-\dot{\mathbf{x}})\cdot\mathbf{n}\rho e + p\mathbf{v}\cdot\mathbf{n} \end{pmatrix} = \hat{\mathbf{F}} - \mathbf{U}\dot{\mathbf{x}} \tag{4-2-3}$$

is the physical flux vector. Here $V(t)$ is the moving control volume and $S(t)$ is the boundary surface surrounding the volume and $\mathbf{n}$ is the normal vector to the surface pointing outward from the control volume, where

$$\mathbf{v} = \begin{pmatrix} u \\ v \\ w \end{pmatrix} \tag{4-2-4}$$

is the velocity of the flow, and

$$\dot{\mathbf{x}} = \begin{pmatrix} \dot{x} \\ \dot{y} \\ \dot{z} \end{pmatrix} \tag{4-2-5}$$

is the velocity of the moving grid.

Here ρ is density, p is pressure, and e is the specific total energy. For a perfect gas, $P = (\gamma-1)\rho(e - \frac{1}{2}\mathbf{v}\cdot\mathbf{v})$ is the state equation of gas, and for air, the ratio of specific heats is $\gamma = 1.4$. The sonic speed c is obtained as $c = \sqrt{\gamma(p/\rho)}$.

4.2.2 Discretization with Finite-Volume-Method (FVM)

Applying the Finite-Volume-Method to Eq.(4-2-6), considering the averaged value of **U** inside the control volume V, we have

$$\frac{\partial(V\mathbf{U})}{\partial t} + \mathbf{R} = 0 \tag{4-2-6}$$

with

$$\mathbf{R} = \int_{S(t)} \mathbf{F}\cdot\mathbf{n}dS \tag{4-2-7}$$

At cell i, a family of two-levels implicit scheme for Eq.(4-2-6) can be obtained as:

$$\frac{V_i^{n+1}\mathbf{U}_i^{n+1} - V_i^{n}\mathbf{U}_i^{n}}{\Delta t} + (1-\alpha)\mathbf{R}_i^{n+1} + \alpha\mathbf{R}_i^{n} = 0 \tag{4-2-8}$$

where n is time level and when $\alpha = 0$, Eq.(4-2-8) is the backward Euler method with 1st order in time. When $\alpha = \frac{1}{2}$, it becomes a Crank-Nicolson method with 2nd order in time.

$$\mathbf{R}_i = \sum_{j\in N(i)} \tilde{\mathbf{F}}_{ij} s_{ij} \tag{4-2-9}$$

is a discretized form of **R** in Eq.(4-2-7), where $N(i)$ means the neighbor cells of cell i, and $\tilde{\mathbf{F}}_{\mathbf{y}}$ is the numerical flux from cell i to cell j and s_{ij} is the area interfacing cell i and cell j.

4.2.3 GCL (Geometry Conservation Law) Satisfaction

To satisfy the Geometry Conservation Law (GCL), a common grid velocity for face S_{ij} between time step n to $n+1$ can be defined as

$$(v_n)_{ij}^{n+1/2} = [\dot{\mathbf{x}}\cdot\mathbf{n}]_{ij}^{n+1/2} = \left(\frac{V_i^{n+1} - V_i^{n}}{\Delta t}\right) \Big/ \left((1-\alpha)s_{ij}^{n+1} + \alpha s_{ij}^{n}\right) = \frac{\Delta V_{ij}^{n+1/2}}{\Delta t\left((1-\alpha)s_{ij}^{n+1} + \alpha s_{ij}^{n}\right)} \tag{4-2-10}$$

where $\Delta V_{ij}^{n+1/2}$ is the swept volume by face S_{ij} from time level n to time level $n+1$. It must be noted that α is included in Eq.(4-2-10).

4.2.4 Dual time stepping [23]

Eq.(4-2-8) represents a nonlinear system of coupled equations that has to be solved at each time step. It can be solved by treating it as a steady-state problem by introducing a

pseudo-time variable τ so that

$$V^{n+1}\frac{\partial \mathbf{U}}{\partial \tau}+\mathbf{R}*(\mathbf{U})=0 \tag{4-2-11}$$

where

$$\mathbf{R}*(\mathbf{U})=\frac{V^{n+1}\mathbf{U}}{\Delta t}+(1-\alpha)\mathbf{R}(\mathbf{U})+\alpha\mathbf{R}^{n}-\frac{V^{n}\mathbf{U}^{n}}{\Delta t} \tag{4-2-12}$$

If Eq.(4-2-11) converged, then Eq.(4-2-8) is satisfied and $\mathbf{U}$ can be taken as $\mathbf{U}^{n-1}$ which has time accuracy as defined in Eq.(4-2-8).

4.2.5 Original LU-SGS Method

For the solution of Eq.(4-2-11), using backward Euler time integration, it can be written as

$$V^{n+1}\frac{\Delta \mathbf{U}^{m}}{\Delta \tau}+\mathbf{R}*(\mathbf{U}^{m+1})=0 \tag{4-2-13}$$

where $\Delta\tau$ is the pseudo-time increment, m is the pseudo-time step, and

$$\Delta\mathbf{U}^{m}=\mathbf{U}^{m+1}-\mathbf{U}^{m} \tag{4-2-14}$$

Eq.(4-2-13) can be linearized in time by setting

$$\mathbf{R}*(\mathbf{U}^{m+1})=\mathbf{R}*(\mathbf{U}^{m+1})+\frac{\partial \mathbf{R}*^{m}}{\partial \mathbf{U}}\Delta\mathbf{U}^{m} \tag{4-2-15}$$

this yields

$$\left[\frac{V^{n+1}}{1-\alpha}\left(\frac{1}{\Delta\tau}+\frac{1}{\Delta t}\right)I+\frac{\partial \mathbf{R}^{m}}{\partial \mathbf{U}}\right]\Delta\mathbf{U}^{m}=-\mathbf{R}^{m}-\frac{V^{n+1}\mathbf{U}}{(1-\alpha)\Delta t}+\frac{1}{1-\alpha}\left(\frac{V^{n}\mathbf{U}^{n}}{\Delta t}-\alpha\mathbf{R}^{n}\right) \tag{4-2-16}$$

or

$$\left[\frac{V^{n+1}}{1-\alpha}\left(\frac{1}{\Delta\tau}+\frac{1}{\Delta t}\right)I+\frac{\partial \mathbf{R}^{m}}{\partial \mathbf{U}}\right]\Delta\mathbf{U}^{m}=\mathbf{Res}^{m} \tag{4-2-17}$$

Following the original LU-SGS [23] approach, $\mathbf{R}$ in the left-hand side is reduced to spatially 1st- order as

$$\tilde{\tilde{\mathbf{F}}}_{\mathbf{ij}}=\frac{1}{2}\left[\mathbf{F}_{i}+\mathbf{F}_{j}-\lambda_{ij}(\mathbf{U}_{j}-\mathbf{U}_{i})\right] \tag{4-2-18}$$

so that,

$$\overline{\mathbf{R}}_{i}=\sum_{j\in N(i)}\tilde{\tilde{\mathbf{F}}}_{\mathbf{ij}}s_{ij}=\sum_{j\in N(i)}\frac{1}{2}\left[\mathbf{F}(\mathbf{U}_{i},\mathbf{n}_{ij})+\mathbf{F}(\mathbf{U}_{j},\mathbf{n}_{ij})-\lambda_{ij}(\mathbf{U}_{j}-\mathbf{U}_{i})\right]s_{ij} \tag{4-2-19}$$

The spectral radius is

$$\lambda_{ij}=\left|\left(\mathbf{v}_{ij}-\dot{\mathbf{x}}_{ij}\right)\cdot\mathbf{n}_{ij}\right|+c_{ij}=\left|\mathbf{v}_{ij}\cdot\mathbf{n}_{ij}-(v_{n})_{ij}\right|+c_{ij} \tag{4-2-20}$$

Solving steps for Eq.(4-2-17) are

step 1: Calculate $\mathbf{D}_{\mathrm{i}}$

$$\mathbf{D}_{i}=\left(\frac{V_{i}^{n+1}}{1-\alpha}\left(\frac{1}{\Delta\tau}+\frac{1}{\Delta t}\right)+\frac{1}{2}\sum_{j\in N(i)}\lambda_{ij}s_{ij}\right)\mathbf{I} \tag{4-2-21}$$

step 2: Forward sweep

$$\mathbf{D}_{i}\Delta\mathbf{U}_{i}^{(*)}=\mathbf{Res}_{i}^{(m)}-0.5\sum_{j\in L(i)}\left\{\left[\mathbf{F}(\mathbf{U}_{j}^{(m)}+\Delta\mathbf{U}_{j}^{(*)},\mathbf{n}_{ij})-\mathbf{F}(\mathbf{U}_{j}^{(m)},\mathbf{n}_{ij})\right]-\lambda_{ij}\Delta\mathbf{U}_{j}^{(*)}\right\}s_{ij} \tag{4-2-22}$$

where $L(i)$ are the neighboring lower side cells

step 3: Backward sweep

$$\Delta\mathbf{U}_{i}^{(m)}=\Delta\mathbf{U}_{i}^{(*)}-0.5\mathbf{D}_{i}^{-1}\sum_{j\in U(i)}\left\{\left[\mathbf{F}(\mathbf{U}_{j}^{(m)}+\Delta\mathbf{U}_{j}^{(*)},\mathbf{n}_{ij})-\mathbf{F}(\mathbf{U}_{j}^{(m)},\mathbf{n}_{ij})\right]-\lambda_{ij}\Delta\mathbf{U}_{j}^{(*)}\right\}s_{ij} \tag{4-2-23}$$

where $U(i)$ are the neighboring upper side cells

step 4: Update $\mathbf{U}$

$$\mathbf{U}_{i}^{(m+1)}=\mathbf{U}_{i}^{(m)}+\Delta\mathbf{U}_{i}^{(m)} \tag{4-2-24}$$

when

$m=0$: $\mathbf{U}^{(m)}=\mathbf{U}^{n}$; and $m=\mathbf{N_{sweep}}$: $\mathbf{U}^{(m+1)}=\mathbf{U}^{\mathbf{n+1}}$.

Repeat steps 1~4 in the pseudo-time for $\mathbf{N_{sweep}}$ times to obtain $\mathbf{U}^{n-1}$.

4.2.6 DP-LUR Method

For an efficient parallel computing, it is desirable to use the neighbor cell values only. A Data-Parallel Lower-Upper Relaxation (DP-LUR) Method [24] is utilized for each pseudo-time step:

$$\begin{aligned}\Delta\mathbf{U}_{i}^{[0]}&=\mathbf{D}_{i}^{-1}\mathbf{Res}_{i}^{(m)}\\ \Delta\mathbf{U}_{i}^{[k]}&=\mathbf{D}_{i}^{-1}\left\{\mathbf{Res}_{i}^{(m)}-0.5\sum_{j\in N(i)}\left\{\left[\mathbf{F}(\mathbf{U}_{j}^{(m)}+\Delta\mathbf{U}_{j}^{[k-1]},\mathbf{n}_{ij})-\mathbf{F}(\mathbf{U}_{j}^{(m)},\mathbf{n}_{ij})\right]-\lambda_{ij}\Delta\mathbf{U}_{j}^{[k-1]}\right\}s_{ij}\right\}\end{aligned} \tag{4-2-25}$$

repeat Eq.(4-2-25) k_{max} times so that

$$\Delta\mathbf{U}_{i}^{(m)}=\Delta\mathbf{U}_{i}^{[k_{\max}]}. \tag{4-2-26}$$

4.2.7 Modified SLAU Scheme for Numerical Flux

There are many schemes to obtain the numerical flux in Eq.(4-2-9). In the AUSM (Advection Upstream Splitting Method)–type scheme [25],

$$\tilde{\mathbf{F}}=\frac{\dot{m}+|\dot{m}|}{2}\mathbf{\Phi}^{L}+\frac{\dot{m}-|\dot{m}|}{2}\mathbf{\Phi}^{R}+\tilde{p}\mathbf{N} \tag{4-2-27}$$

Original SLAU scheme [26, 27] is extended to a moving grid as

$$\mathbf{\Phi}=\begin{pmatrix}1\\u\\v\\w\\h\end{pmatrix}\quad\text{and}\quad\mathbf{N}=\begin{pmatrix}0\\x_{n}\\y_{n}\\z_{n}\\v_{n}\end{pmatrix} \tag{4-2-28}$$

$$h=(e+p)/\rho \tag{4-2-29}$$

v_n calculated with Eq.(4-2-10) must be used to satisfy the GCL.

$$\tilde{p}=\frac{p^{L}+p^{R}}{2}+\frac{\beta^{+}-\beta^{-}}{2}(p^{L}-p^{R})+(1-\chi)(\beta^{+}+\beta^{-}-1)\frac{p^{L}+p^{R}}{2}$$

$$\beta^{\pm}=\begin{cases}\frac{1}{4}\left(2\mp M^{\pm}\right)\left(M^{\pm}\pm 1\right)^{2}, & \left|M^{\pm}\right|<1\\ \frac{1}{2}\left(1+sign(\pm M^{\pm})\right), & \end{cases}$$

otherwise

$$M^{+}=\frac{V_{n}^{L}-v_{n}}{\bar{c}}$$

$$M^{-}=\frac{V_{n}^{R}-v_{n}}{\bar{c}}$$

$$\chi=(1-\hat{M})^{2}$$

$$\hat{M}=\min\left(1.0,\frac{1}{\bar{c}}\sqrt{\frac{(V_{n}^{L}-v_{n})^{2}+(V_{n}^{R}-v_{n})^{2}}{2}}\right)$$

$$\dot{m}=\frac{1}{2}\left\{\rho^{L}\left(V_{n}^{L}+|V_{n}|_{\max}^{+}\right)+\rho^{R}\left(V_{n}^{R}-|V_{n}|_{\max}^{-}\right)-\frac{\chi}{\bar{c}}\Delta p\right\}$$

$$
\begin{aligned}
&|V_n|^{\pm}_{\max} = (1-g)|V_n|_{\max} + g|V_n|^{\pm} \\
&g = -\max(\min(M^{+},0),-1)\cdot\min(\max(M^{-},0),1) \\
&|V_n|_{\max} = \max(|V_n|^{+},|V_n|^{-}) \\
&\Delta p = p^{R} - p^{L} \\
&\bar{c} = \frac{1}{2}\left(c^{L} + c^{R}\right)
\end{aligned}
\tag{4-2-30}
$$

here the speed normal to the face is calculated as

$$
V_n = x_n u + y_n v + z_n w \ . \tag{4-2-31}
$$

$\hat{M}$ in Eq.(4-2-30) is modified from the original form [25] to use the perpendicular velocity component instead of the local total speed at the cell face. In ref. [28], it was pointed out that this might cause instability in the calculations. But with the variables reconstructed with limiters (see next section), no instability was observed from the authors' experience. $\hat{m}$ in Eq.(4-2-30) is more natural and memory saving while applied to a moving grid system.

The SHUS scheme [29] that was applied until recently [30] had some shortcomings, as its numerical dissipation caused unrealistic diversion of its computational results at very low Mach numbers. A two-dimensional drag computation of the NACA 0012 airfoil as shown in figure 35 indicates that the results with the SHUS scheme tend to diverge at Mach numbers lower than 0.1. The SLAU scheme, by contrast, gave realistic drag coefficient values even at very low speeds under Mach 0.01, as well as those at high speed close to, and over Mach 1.

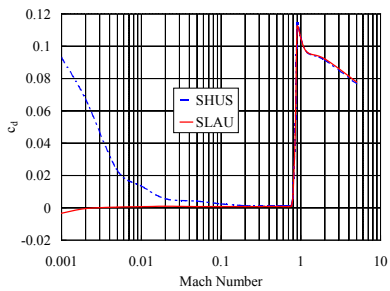

Figure 37. Drag vs. Mach number for NACA 0012 Airfoil

The favorable characteristic of this computational scheme is considered to be well suited to the challenging demands of predicting the flow field surrounding helicopters where a wide range of air speed co-exists.

4.2.8 FCMT for Data Reconstruction

To improve the spatial resolution while keeping the favorable TVD (Total Variations Diminishing) property of the original scheme, a Fourth-order Compact MUSCL TVD (FCMT) interpolation method [31] is used to obtain the L (Left) and R (Right) values at the interfacing face with

$$
\begin{aligned}
q^{L}_{i+1/2} &= q_i + \frac{1}{6}\left(\Delta^{*}\bar{q}_{i-1/2} + 2\Delta^{*}\tilde{q}_{i+1/2}\right) \\
q^{R}_{i+1/2} &= q_{i+1} - \frac{1}{6}\left(2\Delta^{*}\bar{q}_{i+1/2} + \Delta^{*}\tilde{q}_{i+3/2}\right)
\end{aligned}
\tag{4-2-32}
$$

where,

$$
\begin{aligned}
\Delta^{*}\bar{q}_{i-1/2} &= \min\mathrm{mod}\left[\Delta^{*}q_{i-1/2}, b\Delta^{*}q_{i+1/2}\right] \\
\Delta^{*}\bar{q}_{i+1/2} &= \min\mathrm{mod}\left[\Delta^{*}q_{i+1/2}, b\Delta^{*}q_{i+3/2}\right] \\
\Delta^{*}\tilde{q}_{i+1/2} &= \min\mathrm{mod}\left[\Delta^{*}q_{i+1/2}, b\Delta^{*}q_{i-1/2}\right] \\
\Delta^{*}\tilde{q}_{i+3/2} &= \min\mathrm{mod}\left[\Delta^{*}q_{i+3/2}, b\Delta^{*}q_{i+1/2}\right]
\end{aligned}
\tag{4-2-33}
$$

and,

$$
\begin{aligned}
\Delta\bar{q}_{i-1/2} &= \min\mathrm{mod}\left[\Delta q_{i-1/2}, b_1\Delta q_{i+1/2}, b_1\Delta q_{i+3/2}\right] \\
\Delta\bar{q}_{i+1/2} &= \min\mathrm{mod}\left[\Delta q_{i+1/2}, b_1\Delta q_{i+3/2}, b_1\Delta q_{i-1/2}\right] \\
\Delta\bar{q}_{i+3/2} &= \min\mathrm{mod}\left[\Delta q_{i+3/2}, b_1\Delta q_{i-1/2}, b_1\Delta q_{i+1/2}\right]
\end{aligned}
\tag{4-2-34}
$$

and,

$$
\begin{aligned}
\Delta^{*}q_{i+1/2} &= \Delta q_{i+1/2} - \frac{1}{6}\Delta^{3}\bar{q}_{i+1/2} \\
\Delta^{3}\bar{q}_{i+1/2} &= \Delta\bar{q}_{i-1/2} - 2\Delta\bar{q}_{i+1/2} + \Delta\bar{q}_{i+3/2}
\end{aligned}
\tag{4-2-35}
$$

and,

$$
\begin{aligned}
\Delta\bar{q}_{i-1/2} &= \min\mathrm{mod}\left[\Delta q_{i-1/2}, b_1\Delta q_{i+1/2}, b_1\Delta q_{i+3/2}\right] \\
\Delta\bar{q}_{i+1/2} &= \min\mathrm{mod}\left[\Delta q_{i+1/2}, b_1\Delta q_{i+3/2}, b_1\Delta q_{i-1/2}\right] \\
\Delta\bar{q}_{i+3/2} &= \min\mathrm{mod}\left[\Delta q_{i+3/2}, b_1\Delta q_{i-1/2}, b_1\Delta q_{i+1/2}\right]
\end{aligned}
\tag{4-2-36}
$$

here,

$$
\Delta q_{i+1/2} = q_{i+1} - q_i \tag{4-2-37}
$$

In present calculations, $b = 4$, and $b_1 = 2$ is used.

4.2.9 Extension of rFlow3D to complicated configuration

The flow field around a rotor is very complicated and fully unsteady. At the same time, a fuselage, hub system and tail rotor of a helicopter also have complicated configuration. These complicated configurations affects the aerodynamic performance, specifically the power. To solve this kind of problem for a helicopter, special techniques has been adopted in the CFD code [32~34]. So far, JAXA has used the structured grid system around blades, rotor itself. To use the unstructured grid, especially around a complex configuration, makes very easy to handle and construct the grid. To realize this idea, JAXA has been conducting the mutual research cooperation between JAXA and Tohoku University to combine the two grid systems. The Tohoku University supplies their own unstructured code (TAS code). JAXA calls this new combined CFD code as "JANUS code". Figure 38 shows the typical calculation results by JANUS code.

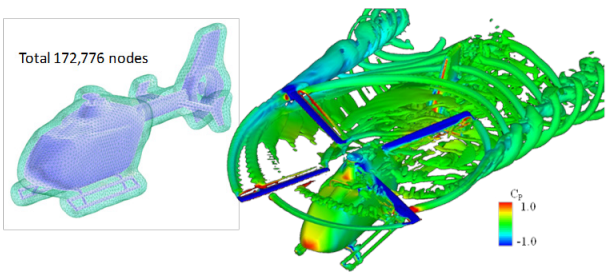

Figure 38. Calculation results by JANUS code.

The comparison of the JANUS results with rFlow3D results has been conducted in figure 39. Figure 39(a) and (b) are results by the rFlow3D and JANUS code respectively. From

these results, there are no differences between them around a fuselage. Figure 39(c) shows the comparison of the pressure distribution across the fuselage by JANUS and rFlow3D code. Still both results show the good correlation about the pressure distribution across the fuselage.

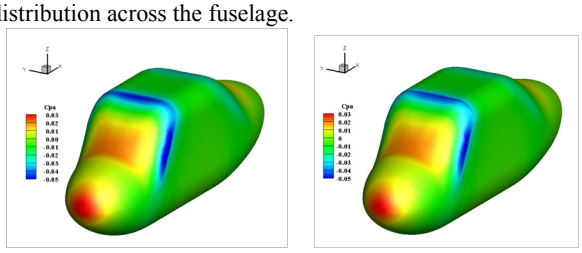

(a) rFlow3D results (b) JANUS results

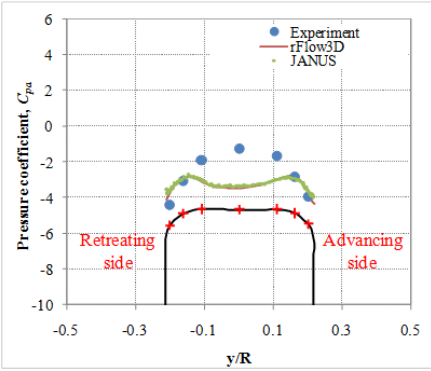

(c) Comparison of the JANUS results with eFlow3D

Figure 39. Comparison of JANUS and rFlow3D results.

4.3 Application of LMT and rFlow3D

In this section, the simulation results by using LCM and rFlow3D will be described.

4.3.1 Gust response of a helicopter [35~37]

Any kind of flying vehicles encounter atmospheric turbulence. In some cases, it causes fatal accident. Therefore it is necessary to investigate the dynamic response of a helicopter. By using the LMT, the dynamic response of a single helicopter has been studied. Figure 40 shows the dynamic response of a rotor which penetrates into the sine-shaped gust. In this figure, there are two results, one is the results of the case of sudden penetration of a rotor into the sine-shaped gust and the other is those by gradual penetration of a rotor. The dynamic response of a rotor in case of sudden penetration shows the phase lead of response compared with those of the case of gradual penetration. As time elapses, both responses will coincident with each other. Figure 41 shows the dynamic response of a rotor for the step-shaped gust. In this case, the difference between sudden and gradual penetration

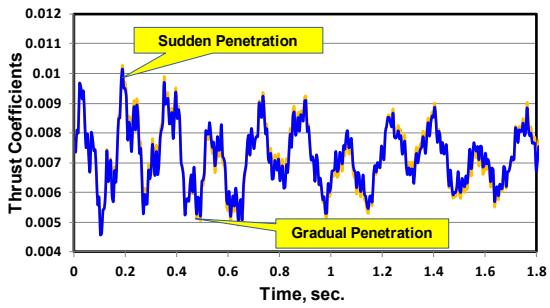

Figure 40. Gust response of a rotor by sine-shaped gust. (Gust frequency=2Hz)

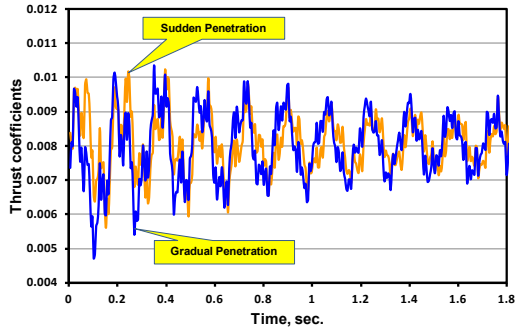

Figure 41. Gust response of a rotor by step-shaped gust

The Gust alleviation system has been developed by means of the optimal control theory [38,39]. Figure 42 shows the results of the gust alleviation. In this figure, the comparison of the several types of control has been shown. The adaptive open-loop control is most effective for gust alleviation.

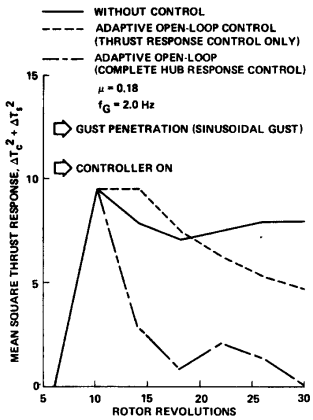

Figure 42. Comparison of the results of several types of control.

In the airport, helicopters sometimes have to crossing a runway to land on the helipad. At the time, helicopters experience the cross or pass nearby the tip vortices generating from the large airplane like a Jumbo Jet. This is a very dangerous aerodynamic interaction between small vehicles such as general aviation or helicopter and large airplanes. In some cases, a small airplane turns over and crashes to the ground.

In such circumstance, it is very important to study the dynamic response of a helicopter which transverse the trajectory of the tip vortices [40~42]. LMT has been applied to investigate these phenomena. Figure 43 show the schematic view between a large jet airplane and a helicopter.

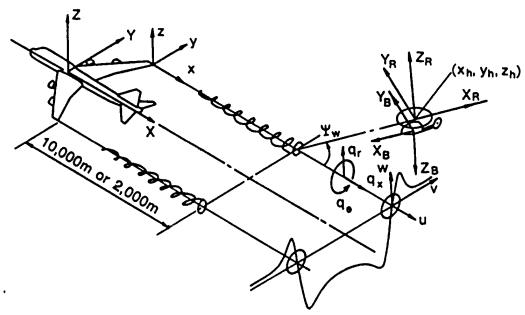

Figure 43. Schematic view of a helicopter which penetrating into the Tip Vortex generated from a large airplane.

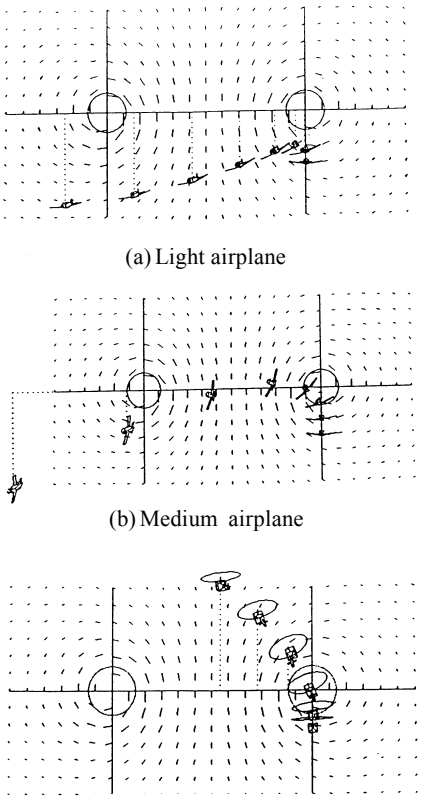

(a) Light airplane

(b) Medium airplane

(c) Helicopter

Figure 44. Comparison of the flight trajectories of the various kinds of vehicle which are penetrating into the tip vortices generated by a large airplane.
(Flight course angle = 0 degree, Flight path angle = 4 degree, Distance = 10,000 m)

Figure 44 shows the calculation example of the dynamic response for small vehicles which are crossing or passing nearby to the tip vortices generated from a large airplane. In this figure, a light airplane could not reach the center of tip vortex and make left turn and for the medium sized airplane the vehicle has completely turned over due to tip vortex. On the other hand, a helicopter could have crossed the tip vortex with small effect on the flight path. From these analytical studies, a helicopter is very safe vehicle compared with the small or medium sized fixed airplane.

4.3.2 Multi-rotor system

4.3.2.1 Aerodynamics for Tandem Rotor helicopter [43,44]

To carry large number of passengers or large amount of layload, the tandem rotor helicopter is the most suitable one. Figure 45 show the CH 47 tandem type helicopter. This kind of helicopter has two rotors which are located fore and aft position like figure 45. Two rotors aerodynamically interact with each other, especially rear rotor always is exposed in the wake of the front rotor. Therefore the rear rotor need more power compared with those of front rotor. Usually tandem type helicopter has two engines. However at the emergency such a one engine operation there is a flight manual how to operate a helicopter. Boeing Company recommends the yawed flight with 10 degrees right yawed angle. In this operation, the rear rotor can used the upwash power of the wake of the front rotor in yawed flight, however for a large yawed angle the parasite drag increases. As a results, the 10 degree yawed angle is selected to be the most effective angle to minimum necessary power of tandem helicopter.

To validate this recommendation in one engine operation, momentum theory has been applied by Stepniewsky. To get more precise information about the wake, the new approach combined the Momentum Theory and Blade Element Theory, named as Local Momentum Theory (LMT), has been developed and applied to this phenomena. This is the main reason to develop the LMT. To apply the LMT to the right yawed flight for tandem rotor, the definition of various kinds axis shown in figure 46 have been adopted.

Figure 45. CH-47 Chinook Tandem Helicopter

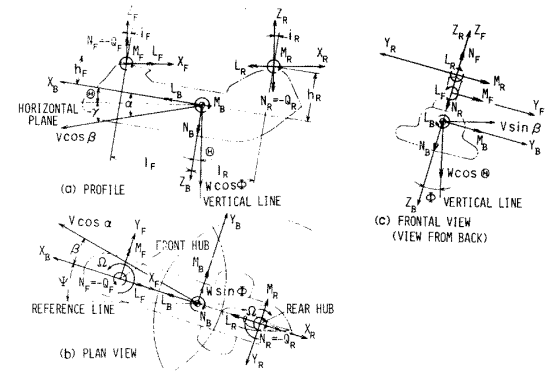

Figure 46. Forces and moments acting on a helicopter

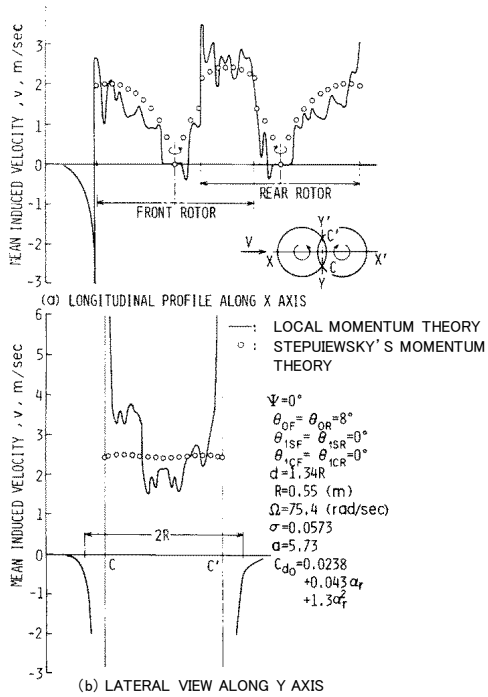

Figure 47. Induced velocities distributions along x axis at hovering flight.

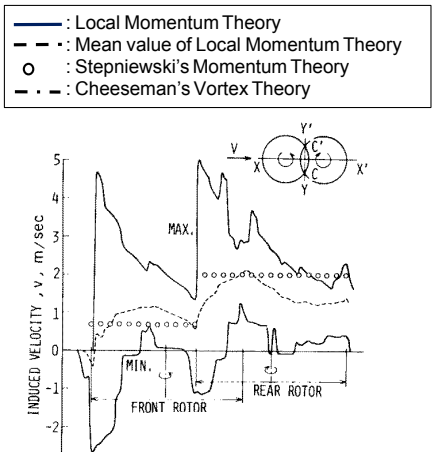

(a) Longitudinal profile along X axis

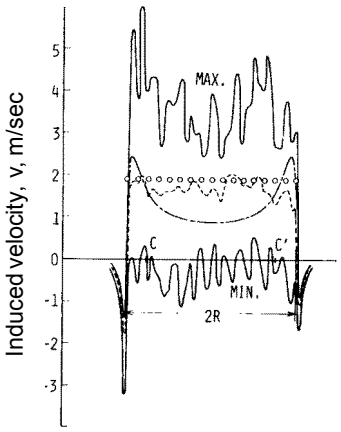

(b) Lateral view along Y axis

Figure 48. Induced velocities distributions along y axis in the forward flight (μ=0.15).

In figure 47 for hovering flight and figure 48 for forward flight, analytical results of LMT and Stepniewsky's Momentum theory have been compared. LMT shows good correlation with Stepniewsky's Momentum Theory and more fluctuated features of the induced velocities. Figure 46 shows the comparison of flight test results with those of LMT and Stepniewsky's Momentum Theory. The power increment by LMT showed the minimum value at the 10 degrees yawed angle, however flight test data shows more decrease of power as right yawed angle increases. The more detail aerodynamic phenomena such as flow separation around the fuselage should be included in this analysis.

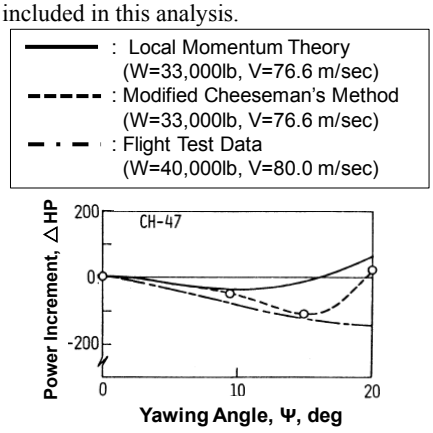

Figure 49. Comparison of theoretical result and flight test data in the power increment due to right yaw.

4.3.2.2 Aerodynamics for Coaxial Rotor helicopter[45,46]

A single rotor helicopter has speed limit due to the aerodynamic characteristics of a rotor. That is caused by the appearance of the reverse flow region at the retreating side of rotor and shock region on the blade at the advancing side. Once this aerodynamic instability has happened, it is very difficult to control a helicopter. To overcome this difficult aerodynamic phenomenon, the new idea like a coaxial type helicopter has been introduced.

Figure 50 shows the demonstrator of coaxial rotor helicopter, S-69. The coaxial rotor helicopter has two rotors up and down and uses a same rotational axis. The rotational direction is reverse to each other. As forward flight speed increases, aerodynamic forces of each rotor mainly are supplied on advancing side of rotor as mentioned before.

For coaxial rotor helicopter was controlled by using these aerodynamic forces on the advancing side. This is why a coaxial rotor helicopter can fly more fast compared with conventional single rotor. To study the aerodynamic characteristics of coaxial rotor helicopter, the model of LMT used in the tandem rotor study has been modified to be handled for coaxial rotor.

Figure 50. Sikorsky S-69 coaxial rotor helicopter.

In the LMT, it is very important to define the attenuation coefficient which specifies the time decay of the induced velocities. Two wake models are arranged in upper and lower position shown in figure 51. These two wake model affect each other. In this wake model, the induced velocity is calculated by adding those of the two wake models. The attenuation coefficient is also calculated by ratio of the induced velocities and it of one step ahead shown in equation (4-1-8).

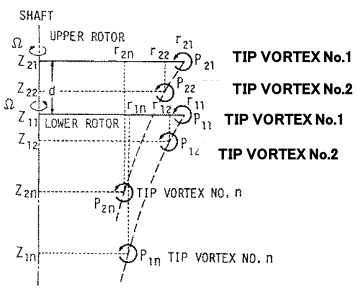

(a) Side view of tip vortices in model

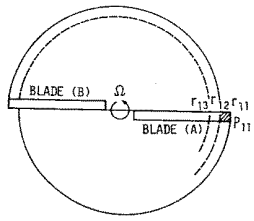

(b) Top view of tip vortices of upper rotor in model

Figure 51. Modeling of the wake geometry used in LMT

analysis.

Using this wake model for coaxial rotor, the rotor performance has been calculated. Figure 52 shows the comparison of the polar curve for a two-bladed single rotor, an hour-bladed single rotor and coaxial rotor with various spacing, d. Thrust coefficient of a coaxial rotor locates between those of a two-bladed single rotor and a four-bladed single rotor. As the spacing distance, d, decreases, rotor performance of a coaxial rotor approaches to that of the four-bladed single rotor. In this figure, the experimental data were also depicted and compared with those of the theoretical results. The calculated results by LMT show the excellent correlation to the experimental data. Figure 53 also shows the comparison between LMT results and experimental data for the upper and lower rotor. The calculation results by LMT show the good correlation to the experimental data.

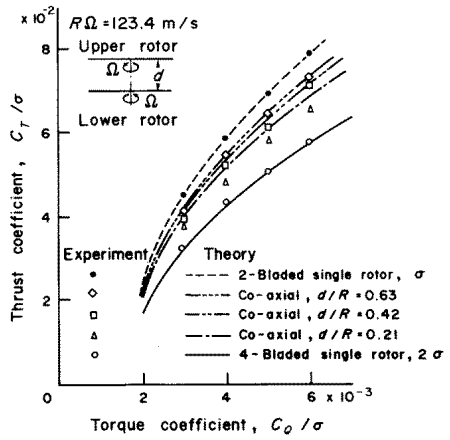

Figure 52. Polar curves for various rotor clearances

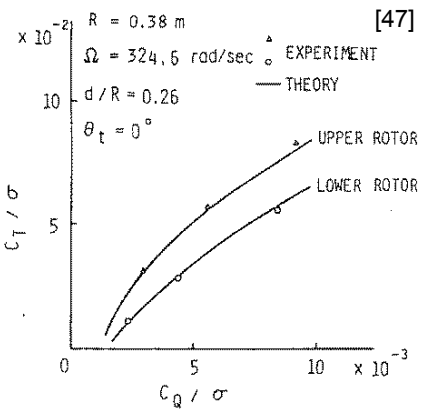

Figure 53. Comparison of the polar curve of the theoretical results with experiments.

4.3.3 Propeller Analysis

4.3.3.1 Advanced Turbo Prop (ATP) propeller [48~55]

In 1970, the price of petroleum has been getting high. According this increase of the consuming price of petroleum, almost every price has been going up. Of course, the airfare of commercial airplane was getting high. This situation was unusual for ordinary people. The engine companies have to create the new type of engine compared with conventional jet engine. The Advanced Turbo Prop engine has been introduced instead of the conventional jet engine. This type of propeller operates in the high subsonic speed range (Mach No.=0.7~0.8). The jet engine has rotor with fan blades inside of the fairing. Therefore Advanced Turbo Prop engine was same idea as those to remove the fairing at the rotor region of the conventional engine. This is why this type of propeller is called as an open rotor. Usually the rotor of an engine is single stage. So Single Rotating Propeller (SRP) has been investigated in order to evaluate its rotor efficiency. Figure 54 shows the schematic view of SRP. Euler code has been applied to analyze the flow field around a SRP.

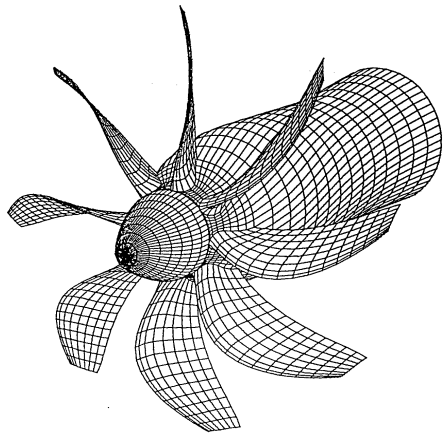

Figure 54. Single Rotating Propeller (SRP).

Figure 55 shows the comparison of the CFD results with experiment for a SRP. In this figure, two calculation results are depicted together, one is the Euler calculation and the other is Navier-Stokes calculation. The effect of the skin friction is remarkable. The results of Navier-Stokes calculation show excellent agreement with experiment.

On the other hand, figure 56 shows the calculation results for a Counter Rotating Propeller (CRP). In the case of the CRP, the rear rotor can absorb the swirl energy generated by the fore rotor. Therefore compared with SRP, CRP shows more efficient performance. Figure 57 shows the comparison of the CFD result with the experimental data. In this figure, only one case has been conducted for comparison. Both results show good correlation to each other.

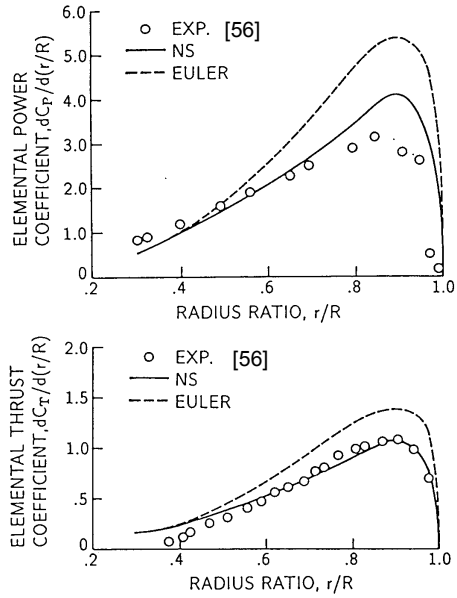

Figure 55. Comparison of radial distributions of predicted and measured performance

$(M_\infty = 0.8, \beta_{0.75R} = 60.5°, J = 3.06, R_e = 1.95 \times 10^6)$

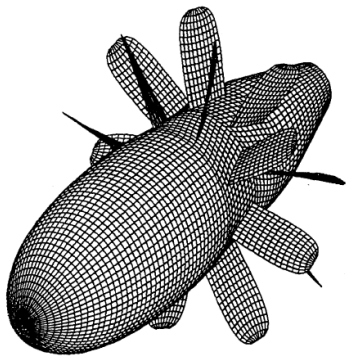

Figure 56. Schematic view of a counter-rotating propeller.

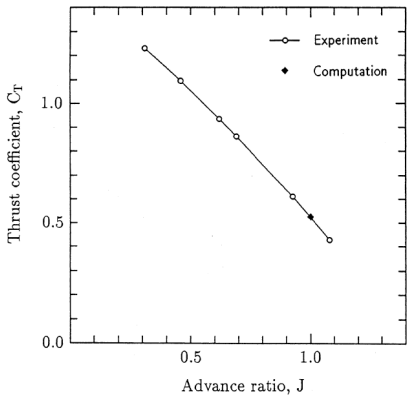

Figure 57. Comparison of the Thrust coefficient with experimental data [56].

($Mach\ no.$ = 0.2, $Advance\ Ratio$ = 1.0, Re = $5X10^5$, θ_{0F} = 36°, θ_{0R} = 32°)

4.3.4 Noise analysis by rFlow3D

4.3.4.1 HSI noise analysis [57,61]

The noise reduction is most important issue for a civil-used helicopter. Among several kinds of noise, HSI and BVI noises are most impulsive and annoying for human, especially people living near the heliport. JAXA has conducted the helicopter noise research for several years.

As the forward speed of a helicopter increases, a blade itself experiences the transonic speed regime near blade tip region in the advancing side. As the relative speed goes to Mach number 1.0, the shock on an advancing blade has been generated. High Speed Impulsive (HSI) noise is generated by the shock on the blade and its level is depending on the strength of this shock. HSI noise is propagating by the small perturbation of the shock region on a blade at the tip region. The noise directivity is straight forward of a rotor. It is well known that HSI noise can reaches to the far from a helicopter.

During research period, JAXA has developed the CFD analysis code to calculate the flow field around the helicopter rotor.

To study the noise problem of a helicopter, JAXA has developed the CFD analysis code to calculate the flow field around a helicopter rotor, which is composed of a noise analysis code to calculate the pressure fluctuation at the observer position and finally post-processing code to draw the noise contour or pressure distribution on the blade or fuselage etc. Figure 58 shows the Grid system in the CFD calculation to analyze the HSI noise at hover. The cylindrical grid around a blade has constructed including the blade tip region.

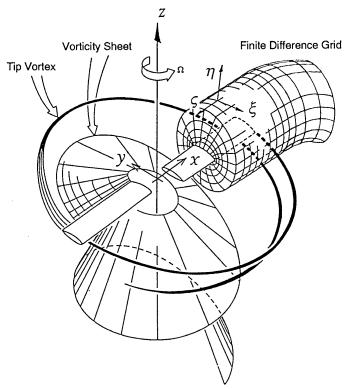

Figure 58. Grid system for HSI noise analysis

To calculate the pressure fluctuation at the observer position, the Kirchhoff equations has been adopted as wave formulation. In figure 59, the Kirchhoff surface for this noise analysis is shown. Figure 60 shows the calculation results for HSI noise. The feature of the spike deeply depends on the location of the Kirchhoff surface. In this calculation, the value of 1.14R (R is a rotor radius) in the spanwise direction was selected.

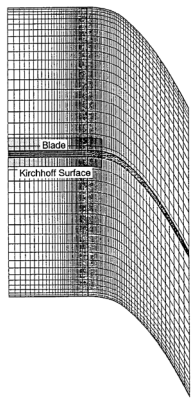

Figure 59. Kirchhoff surface around a blade

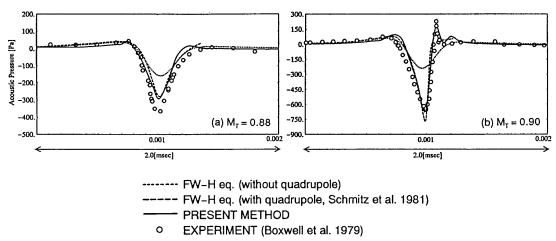

Figure 60. Acoustic pressure in non-lifting hover condition

(Wing section : NACA0012, AR = 13.71, source position : in - plane, r/D = 1.5)

On the other hand, in forward flight case, Ffowcs-Williams Hawkings formulation has been adopted because of the unsteady pressure distributions on a blade. Figure 61 show the iso-Mach contour around a blade. In the figure, the velocity measured in the rotating frame is shown for a blade at the advancing side of a rotor. And also, there can be seen that small spot (shock region) on a blade near the tip region. The small perturbation of the shock region propagates to the outside of a blade. In the right figure of figure 61, this small spot has connected with the outer region which velocity exceeds the sound velocity. This phenomenon is called as 'Delocalization' and depends on the relative velocity to a blade. HSI noise suddenly becomes louder after this delocalization

has happened.

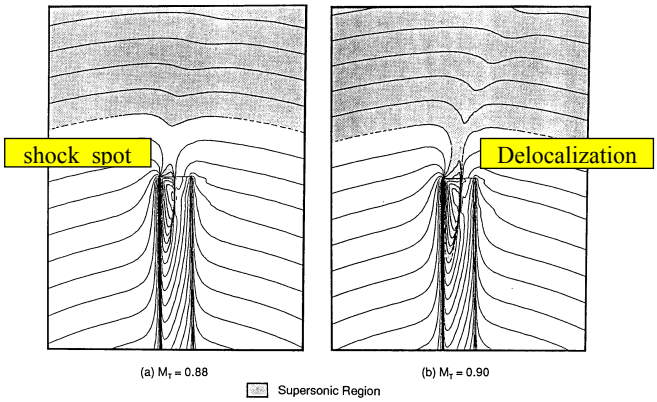

Figure 61. Iso-Mach contour around a blade tip

Figure 62 shows the comparison of the CFD results between JAXA and MHI calculation for the wind tunnel test. The calculation results of both institutes show the good correlation with experimental data, but both results did not show the steep spike of pressure recovery. Both institutes used the Kirchhoff equation to calculate the noise wave at the observer position. The shape of this spike strongly depends on the boundary position of the Kirchhoff surface used in this calculation.

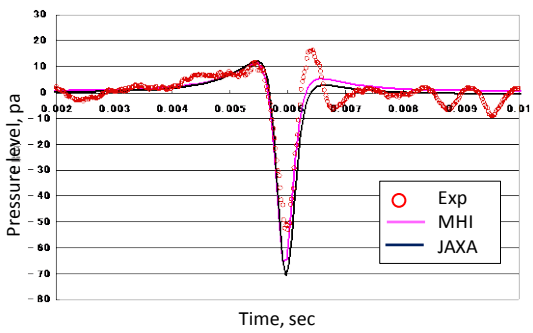

Figure 62. Comparison of the CFD results between JAXA and MHI.

4.3.3.2 BVI noise analysis [62,75]

When helicopter is descending or approaching to the landing spot, tip vortices generated from preceding blade tip region hit the blades shown in figure 63. At this time, the very impulsive and annoying noise is generated. This noise is called as Blade Vortex Interaction (BVI) noise. To analyze the blade vortex interaction, JAXA has developed the CFD code, in which the overlapped grid method has applied in this code. Figure 64 shows the overlapped grid system in this analysis. In these grids, inner grid is very important because the wake structure should be captures more precisely.

By using this CFD code, the calculations have been conducted at the BVI condition. Figure 65 shows the typical result of wake systems which were generated by a rotor. The tip vortices were clearly captured in this analysis. From this figure, it is shown that the tip vortices rolls up as the flow goes down stream.

To calculate the sound pressure level at the observer position, the Ffocks-Williams and Hawkings formulation has been applied. In the noise analysis, the retarded time is very important in the calculation. Figure 66 shows the interference sphere which was used in the noise calculation. In the sound calculations, Farassat 1 formulation has been used.

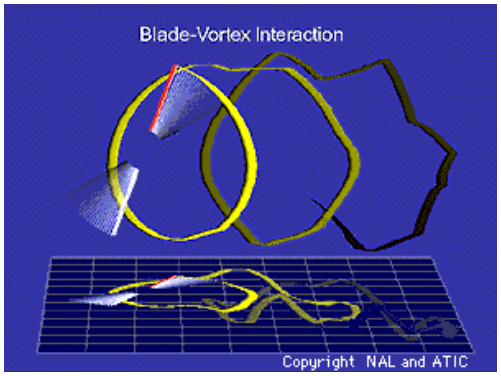

Figure 63. Schematic view of tip vortices from blade tip.

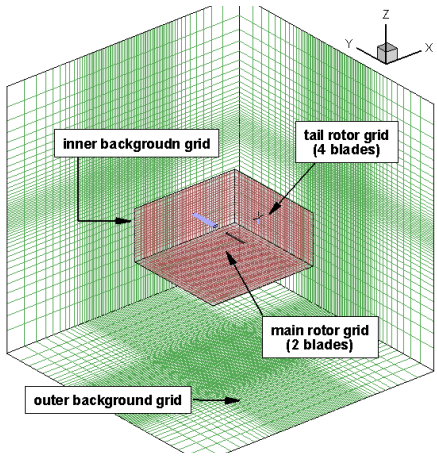

Figure 64. Grid system used BVI analysis (Overlapped Grid System)

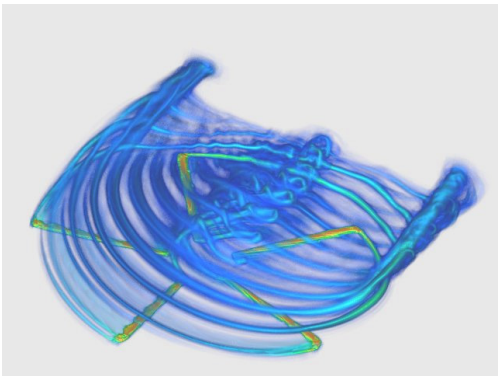

Figure 65. Rotor wake system calculated by JAXA code

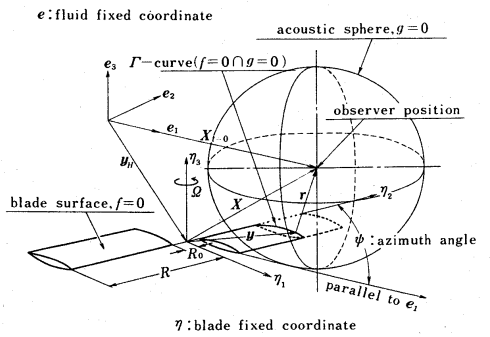

Figure 66. Interference sphere for FW-H formulation.

Figure 67 and 68 show the comparison of BVI noise by CFD analysis and experimental data. Both results show the good correlation, but CFD results show under-prediction compared with experiment. This is because the capturing of the tip vortices in the space was poor. The accuracy of BVI noise always depends on the resolution of the grid system. In figure 68, this wind tunnel has been conducted by the Advanced Technology Institute for commuter Helicopter (ATIC).

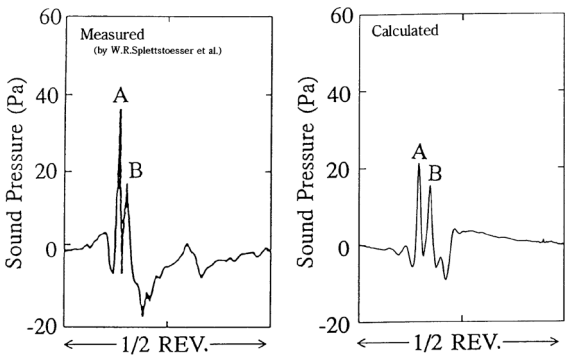

Figure 67. Comparison between measured and calculated time histories of BVI noise.

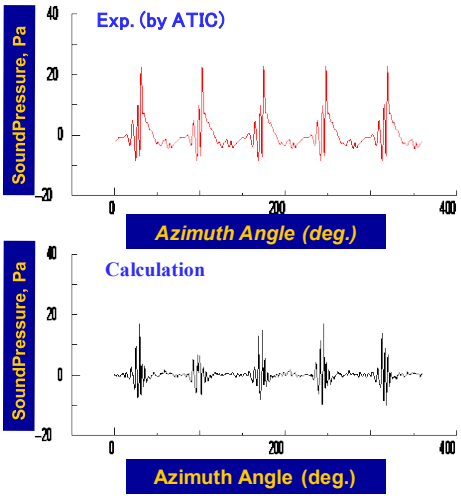

Figure 68. Comparison of the CFD calculation with the ATIC wind tunnel test data.

Figure 69 shows the carpet contour on the plain underneath the rotor. It is clear that the BVI noise mainly occurs in the first quadrant of the rotor. From this study, JAXA has developed the helicopter rotor noise analysis system shown in figure 70.

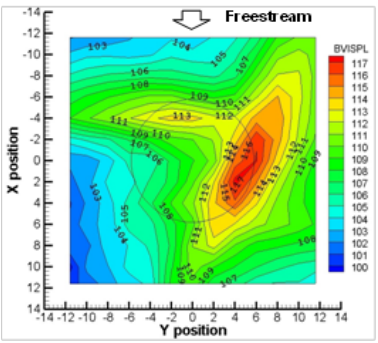

Figure 69. Noise carpet (BVISPL) for baseline blade.

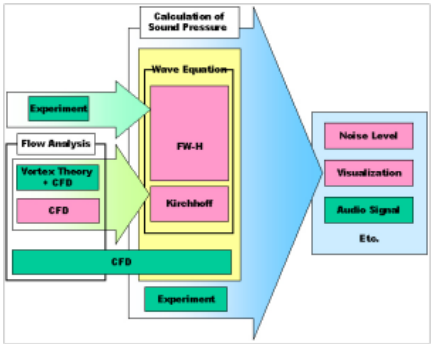

Figure 70. The chart of acoustic analysis.

4.3.3.3 Rotor-Fuselage interaction analysis [76~78]

JAXA has conducted the wind tunnel test to investigate the interference between rotor wake and fuselage in JAXA 6.5x5.5 Low Speed wind tunnel. In this section, the effect of the hub configuration on the aerodynamic characteristics of the surface pressure on a fuselage has been shown in figure 71 and 72. The existence of the rotor hub has great effect on the pressure distribution on fuselage surface, especially just beneath the rotor. The figure (b) in figure 71 shows the very complicated flow field around the hub region.

The time averaging techniques for the unsteady pressure distribution has been used in this analysis.

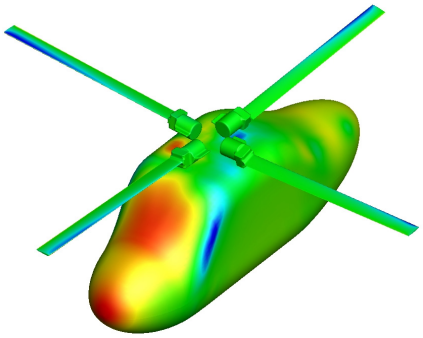

(a) Pressure contour on the fuselage surface

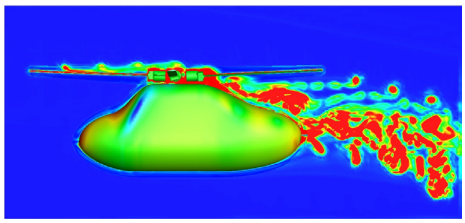

(b) Iso-vorticity contour around the fuselage with rotor hub.

Figure 71. Calculated results by rFlow3D

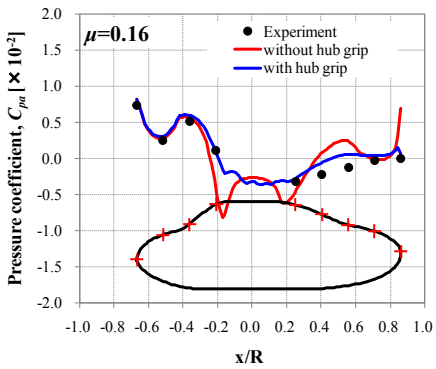

(a) Pressure distribution along the center line.

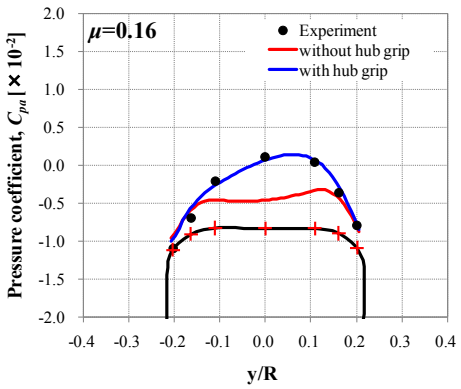

(b) Pressure distribution across the fuselage

Figure 72. Comparison of the pressure distribution by with hub and without hub.

4.3.4 Development of the Water Cannon for helicopter

JAXA has responsibility to meet the social requirement in the aeronautics field. In 1988, the fire accident of the high building has occurred in Tokyo shown in figure 73. However at the time, Tokyo Fire Department has no means to rescue residents for evacuation from the fire accident even though they have helicopters. Under circumstances, Tokyo Fire Department took action to have the internal committee to discuss how to use the helicopter in such fire accident of high building.

Tokyo Fire Department has aviation unit in Tokyo Tachikawa-base. They have 7 helicopters including two medium sized helicopters. In 1990, they started the project for the developing the fire fighting system using water cannon which should be onboard of medium-sized helicopter [79,80]. The members of the committee were composed by professors, researchers, operators and government officers. In the committee, several important issues such as the investigation of the characteristics of winds around buildings, the operation schemes in order to hover near a building, theoretical simulation about the accuracy rate to hit the target (in this case, windows) and those by simulator, and flight tests. JAXA has involved from the beginning of the project as members of this committee and played an important role in this feasibility study.

Figure 74 shows the wind measuring points around the real building. One position located in the windward position, the other position located the leeward position. The height of a building were lower portion (10 m) and higher portion (40 m). The measuring data of wind was analyzed by Fourier analysis and the mathematical wind model was established using these wind data . By using this mathematical wind model, the simulator test has been conducted in JAXA. In the simulator test, two types of control system, one is Safety Augmented System (SAS) and the other is Automatic Stability Equipment (ASE), are installed on a helicopter.

Figure 75 shows the results of simulator test, in which the size of target was assumed to be 2 m x 2 m squares (windows). Rigid line shows the fluctuation of a helicopter in windy circumstance. Figure (a) of figure 75 shows the flight test data and (b) shows the flight simulator test results. From these two figures, the simulator results of a helicopter has shown the very reasonable results. From these results, the mathematical wind model is well simulating the real wind and as a result, the trajectory of a helicopter in wind around a high building has a good correlation with the simulator test results.

Figure 73. The fire of the high building and the rescue activity for a resident from the top roof of a building.

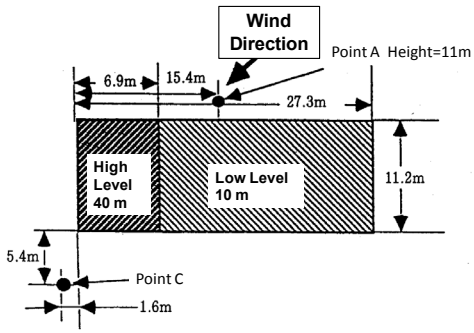

Figure 74. Wind measurement position around real building.

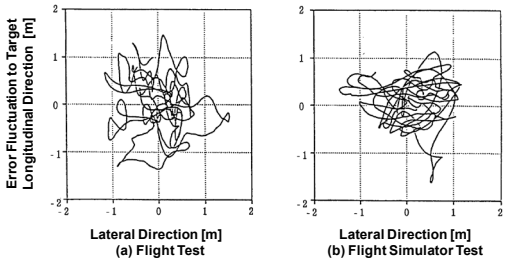

Figure 75. Comparison of the simulation results with flight test.

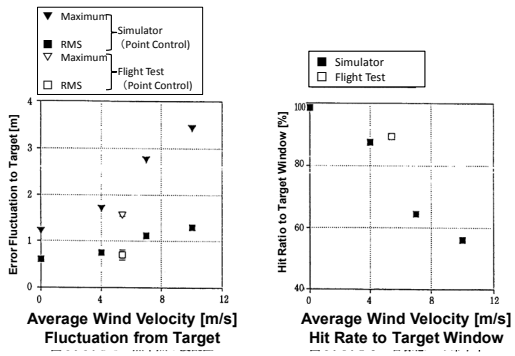

Figure 76. Error evaluation of the hit rate for fire-fighting helicopter against the wind velocities.

Figure 76 also shows the error evaluation of the hit rate against wind velocities. As the velocity of wind increases, the missing rate to the target window was getting high. The wind velocity of 7 m/s was the limit to fly around building for the

activity of fire extinguishment of helicopters. After more precise feasibility study for the fire-fighting helicopter with fire cannon, the real-sized fire-fighting helicopter has developed in 1998. Figure 77 shows the photograph of the training for fire extinguishment of fire-fighting helicopter in case of the fire of a high building.

Figure 77. Photograph of the training of the fire-fighting helicopter with water cannon onboard of a helicopter

5. COLLABORATION INSTITUTES AND COMPANIES ON RESEARCH

JAXA has conducted various collaborations with companies listed below so far.

(a) Domestic companies:
Mitsubishi Heavy Industry (MHI)
Kawasaki Heavy Industry (KHI)
Fuji Heavy Industry (FHI)
Ishikawajima-Harima Heavy Industry (IHI)
Kawada Industry
Yamaha Motor Company. LTD

And universities:
(b) Universities
Tokyo University
Tohoku University
Nagoya University
Kyusyu University
Kobe University
Nihon University
Tokai University.

These institutes have their unique potentials and talents in technologies and researchers. JAXA has been greatly supported from them and encouraged through the deep discussion with them.

On the other hand, JAXA has conducted the international collaboration with so many international institutes including the national laboratories and foreign universities such as :

(c) International institutes
NASA
ONERA
DLR
KARI
KAIST
Konkuk University
Seoul National University
Busan National University.

JAXA has also been greatly stimulated by the advanced technologies and new ideas though the papers or direct discussions and communications. Specifically JAXA is now a member of the on-going international project called as 'STAR Project'. As a member of this international project, JAXA would like to fulfill our responsibility.

6. CONCLUSIONS

In this paper, the histories of JAXA helicopter research have been described. JAXA has mainly focused on the two subjects, one is the equipment of the rotor test stands, and the other is the development of theoretical analysis codes such as Momentum theory, Local Momentum Theory (LMT), Local circulation Method (LCM), prescribed wake theory, CFD code (rFlow3D) suing Euler formulations and Navier-Stokes formulations. By using these tools, JAXA has conducted helicopter research in order to understand the physical phenomena and meaning for several problems. During research terms, JAXA has conducted so many cooperation with various kinds of domestic and international institutes. They are so helpful and fruitful collaborations for JAXA research works. The results come from these collaborations have been applied to the new ideas to be developed equipments or to understand phenomena.

ACKNOWLEDGMENTS

The authors express their great thanks to all people who were involved in the wind tunnel tests and theoretical discussions in domestic and international helicopter researchers of institutes in the world. Especially we would like to appreciate very much Professor Akira Azuma who always advices us and makes lead us to the proper ways in the helicopter research fields.

REFERENCES

[1] http://www.jaxa.jp/
[2] M. Shirai, T. Suenaga, S. Saito, S. Baba, O. Nonaka, N. Adachi, H. Kato and M. Harada, "Equipment of the Multi-purpose High Speed Rotary test Stand in NAL", 66th Hudou Kenkyu Kaigi, 2001, un Japanese.
[3] N. Kobiki, S. Saito, "About One-bladed Rotor test Stand", 73th Hudou Kenkyu Kaigi, 2004, in Japanese.
[4] M. Nakao, N. Uchiyama, K. Takenaka, H. Suzuki, S. Saito and T. Aoyama, "High Speed Impulsive Noise", 34th Aircraft Symposium, Numerical simulation Symposium for aeronautics and space 2001, June, 2001, in Japanese.
[5] T, Suenaga, M. Shirai, S. Saito, O. Nonaka, H. Hosino, S. Baba and K. Murota, "Basic Research of Active Flap Effects on Wing in the NAL Low-Speed Wind Tunnel", 66th Hudou Kenkyu Kaigi, 1999, in Japanese.
[6] I. Maeda, N. Adachi, M. Nakao, N. Kondo, T. Suenaga, S. Baba and S. Saito, "Measurement of BVI noise of a helicopter rotor in NAL 6.5 m x 5.5 m Low Speed Wind Tunnel, 69th Hudou Kenkyu Kaigi, 2002, un Japanese.
[7] N. Kobiki, N. Kondo, S. Saito, T. Akasaka, Y. Tanabe, "Active Tab, a New Active Technique for Helicopter Noise Reduction", 29th European Rotorcraft Forum, Friedrichshafen, Germany, September 16-18, 2003.
[8] N. Kobiki, T. Akasaka, N. Kondo, Y. Tanabe, and S. Saito, "An Experimental Study of On-blade Active Tab for Helicopter Noise Reduction", 30th European Rotorcraft Forum, Marseilles, France, September 14-16,

2004.
[9] N. Kobiki, S. Saito, T. Akasaka, Y. Tanabe, H. Fuse, "An Experimental Study for Aerodynamic and Acoustic Effects of On-blade Active Tab", 31st European Rotorcraft Forum, Italy, September, 2005.
[10] N. Kobiki, S. Saito, M. Kosaka, H. Fuse, "A Study of Closed Loop Control of Active Tab with BVI Detection Method for Helicopter Noise Reduction", 32nd European Rotorcraft Forum, Maastricht, The Netherlands, September 12-14, 2006.
[11] N. Kobiki, S. Saito, T. Fukami and T. Komura, "Design and Performance Evaluation of Full Scale On-Board Active Flap System". American Helicopter Society 63th Annual Forum, Virginia Beach, VA, May 2007.
[12] N. Kobiki, S. Saito, H. Fuse, "A Study of Closed Loop Control for BVI Noise Reduction by Multiple pressure sensors", 33rd European Rotorcraft Forum, Kazan, Russia, September 11-13, 2007.
[13] N. Kobiki, and S. Saito, "Performance Evaluation of Full Scale On-Board Active Flap System in Transonic Wind Tunnel". American Helicopter Society 64th Annual Forum, Montreal, Canada, April 2008.
[14] Y. Tanabe, S. Saito, N. Kobiki, K. Murota, H. Sugawara, K. Hayashi and K. Hiraoka, "An Experimental Study of Rotor/Fuselage Interaction", 35th European Rotorcraft Forum, Hamburg, Germany, September 22-25, 2009.
[15] Y. Tanabe, S. Saito and I. Otani, "Numerical Simulations of Rotor/Fuselage Interactions Utilizing an All-Speed Scheme", 2nd International Forum on Rotorcraft Multidisciplinary Technology, Seoul, Korea, October 19-20, 2009.
[16] Y. Tanabe and S. Saito, "Experimental and Numerical Studies of Rotor/Fuselage Interactions", American Helicopter Society Aeromechanics Specialists' Conference, San Francisco, California, Jan. 20-22, 2010.
[17] Y. Tanabe and S. Saito, "Validation of a New Rotor Flow Code Using JMRTS Experimental Data", American Helicopter Society 66th Annual Forum, Phoenix, AZ, May 11-13, 2010.
[18] A. Azuma and K. Kawachi, "Local Momentum Theory and Its Application to a Rotary Wing", AIAA 75-865, 1975.
[19] A. Azuma and K. Kawachi," Local Momentum Theory and Its Application to a Rotary Wing", Journal of Aircraft, Vol. 16, No. 16. pp.6-14, 1979.
[20] A. Azuma, K. Nasu and T. Hayashi, An Extension of the Local Momentum Theory to Rotors Operating in a twisted Flow Field, Vertica, Vol. 7, pp. 45-59, 1983.
[21] Y. Tanabe and S. Saito S, "Significance of All-Speed Scheme in Application to Rotorcraft CFD Simulations", The 3rd International Basic Research Conference on Rotorcraft Technology, Nanjing, China, October 14-16, 2009.
[22] H. Luo, J. Baum & R. Lohner, "On the Computation of Multi-Material Flows Using ALE Formulation", Journal of Computational Physics, Vol.194, pp.304–328, 2004.
[23] L.P. Zhang & Z.J. Wang, "A Block LU-SGS Implicit Dual Time-Stepping Algorithm for Hybrid Dynamic Meshes", Computers & Fluids, Vol.33, pp.891–916, 2004.
[24] M.J. Wright, G.V. Candler & M. Prampolini, "Data-Parallel Lower-Upper Relaxation Method for the Navier-Stokes Equations", AIAA Journal, Vol.34, No.7, July 1996, pp.1371-1377.
[25] M.S. Liou, "A Sequel to AUSM, Part II: AUSM+-up for All Speeds", Journal of Computational Physics, Vol.214, pp.137-170, 2006.
[26] E. Shima & K. Kitamura, "On New Simple Low-Dissipation Scheme of AUSM-Family for All Speeds", 47th AIAA Aerospace Sciences Meeting, Orlando, FA, January 5-8 2009, AIAA Paper 2009-136.
[27] E. Shima & K. Kitamura, "On AUSM-Family Scheme for All Speeds with Shock Detection for Carbuncle-Fix", 19th AIAA CFD, 22-25 June 2009, San Antonio, Texas, AIAA Paper 2009-3544.
[28] E. Shima & K, Kitamura, "On New Simple Low-Dissipation Scheme of AUSM-Family for All Speeds", 47th AIAA Aerospace Sciences Meeting, Orlando, FA, January 5-8 2009, AIAA Paper 2009-136.
[29] E. Shima & T. Jounouchi, "Role of CFD in aeronautical engineering (No.14) - AUSM type upwind schemes - ", NAL SP-34, 1999, pp.7-12.
[30] Y. Tanabe & S. Saito, "A Simplified CFD/CSD Loose Coupling Approach for Rotor Blade Deformation", JAXA-RR-08-008E, 2009.
[31] Yamamoto, S. and Daiguji, H., Higher-Order-Accurate Upwind Schemes for Solving the Compressible Euler and Navier-Stokes Equations, Computers & Fluids, Vol.22, No.2/3, pp.259-270, 1993.
[32] Y. Tanabe and S. Saito, "Validation of a New Rotor Flow Code Using JMRTS Experimental Data", American Helicopter Society 66th Annual Forum, Phoenix, AZ, May 11-13, 2010.
[33] Y. Tanabe, S. Saito, O. Takayama, D. Sasaki and K. Nakahashi, "A New Hybrid Method of Overlapping Structured Grids Combined with Unstructured Fuselage Grids for Rotorcraft Analysis", 36th European Rotorcraft Forum, Paris, September 7-9, 2010.
[34] Y. Tanabe and S. Saito, "Improvements in Noise Prediction for Rotorcraft", HeliJapan 2010, Omiya, November 1-2, 2010.
[35] S. Saito, "Study of Gust Response of a Helicopter", Doctoral Thesis, March, 1980.
[36] A. Azuma and S. Saito, "Study of Rotor Gust Response by means of the Local Momentum Theory", Journal of American Helicopter Society, January, 1982.
[37] S. Saito, A. Azuma and M. Nagao, "Gust Response of Rotary Wing and Its Alleviation," Vertica, Vol. 5, No. 2, pp. 173-184, 1981.
[38] S. Saito, "A Study of Helicopter Gust Response Alleviation by Automatic Control", NASA TM 85870, December, 1983.
[39] S. Saito, "Application of an Adaptive Blade Control Algorithm to a Gust Alleviation System", Vertica, Vol.8, No.3, pp.289-307, 1984.
[40] S. Saito, A. Azuma, K. Kawachi and Y. Okuno, "Study of the Dynamic Response of Helicopter to a Large Airplane Wake", 12th European Rotorcraft Forum, Paper No.42, Garmisch-Partenkirchen, FDR, September 1986.
[41] A. Azuma, S. Saito and K Kawachi, "Response of Helicopter Penetrating the Tip Vortices of Large Airplane", Vertica, Vol.11, No.1/2, pp.65-76, 1987.
[42] S. Saito, A. Azuma, Y. Okuno and T. Hasegawa, "Numerical Simulations of Dynamic Response of Fixed- and Rotary Wing Aircraft to a Large Airplane Wake", 13th European Rotorcraft Forum, Paper No.7-1, Arles, France, September 8-11, 1987.
[43] A. Azuma, S. Saito, K. Kawachi and T. Karasudani, "Application of the Local Momentum Theory to the Aerodynamic Characteristics of Tandem Rotor in Yawed Flight", 4th European Rotorcraft and Powered Lift Aircraft Forum, Paper No.4, Stresa, Italy, September 1978.

[44] A. Azuma, S. Saito, K. Kawachi and T. Karasudani, "Application of the Local Momentum Theory to the Areodynamic Characteristics of Multi-Rotor Systems", Vertica, Vol.3, No.2, pp.131-141, 1979.
[45] S. Saito, "A Numerical Approach to Co-Axial Rotor Aerodynamics, 7th European Rotorcraft and Powered Lift Aircraft Forum, Paper No.42, Garmish-Parterkirchen, Federal Republic of Germany, September 1981.
[46] S. Saito, "A Numerical Approach to Co-Axial Rotor Aerodynamics", Vertica, Vol.6, No.4, pp.253-266, 1982.
[47] T. Nagashima, H. Ouchi and F. Sasaki, "Optimal Performance and Load Shearing of Co-axial Rotor in Hover", J. of Japan Society for Aeronautics and Space Sciences, Vol.26, No.293, June, 1978, in Japanese.
[48] S. Saito, H. Kobayashi, Y. Wada and Y. Matsuo, "Numerical Approach of Advanced Turboprop with Three-Dimensional Euler Equations", First International Pacific Air and Space Technology Conference, SAE-872448, Melbourne, Australia, November 13-17, 1987.
[49] Y. Matsuo, S. Saito, C. Arakawa and H. Kobayashi, "Navier-Stokes Computations for Flowfield of an Advanced Turboprop", 24th AIAA/ASME/SAE/ASEE Joint Propulsion Conference, AIAA-88-3094, Boston, USA, July 11-14, 1988.
[50] S. Saito, Y. Nakamura, H. Kobayashi and Y. Matsuo, "Predicted Flow Field Around the Advanced Propeller at Take-off", 24th AIAA/ASME/SAE/ASEE Joint Propulsion Conference, AIAA-88-3151, Boston, USA, July 11-14, 1988.
[51] Y. Mastuo, S. Saito, C. Arakawa and H. Kobayashi, "Navier-Stokes Simulations Around a Propfan using Higher-Order Upwind Scheme". 25th AIAA/ASME/SAE/ASEE Joint Propulsion Conference, AIAA-89-2699, Monterey, U.S.A., July 10-14, 1989.
[52] K. Nasu, S. Saito, H. Kobayashi and Y. Nakamura, “Extension of Local Circulation Method to Counter Rotation Propeller, SAE 87-1891.
[53] S. Saito, H. Kobayashi, K. Nasu and Y. Nakamura, "Performance Calculation of Counter Rotation Propeller", 23rd AIAA/SAE/ASME/ASEE Joint Propulsion Conference, AIAA-87-1889, San Diego, USA, June 29 - July 2, 1987.
[54] S. Saito, H. Kobayashi and Y. Nakamura, Performance Calculation of Counter Rotation Propeller, SAE 87-1889.
[55] K. Nasu, and A. Azuma, An Experimental Verification of the Local Circulation Method for a Horizontal Axis Wind Turbine, 18th Inter Society Energy Conversion Engineering Conference, pp. 21-26, August, 1983.
[56] Y. Matsuo and S. Saito, "Numerical Analysis of Three-dimensional viscous flows around an advanced conterrotating Propeller, ICAS-92, Beijing, People's Republic of China, September20-25, 1992.
[57] T. Aoyama, S. Saito, K. Kawachi and J. Kamio, "Unsteady Analysis of Transonic Helicopter Rotor Noise", 19th European Rotorcraft Forum, Cernobbio (Como), September 14-16, 1993.
[58] S. Saito, T. Aoyama, K. Kawachi and J. Kamio, "Aeroacoustic Analysis of Transonic Helicopter Rotor Noise", International Pacific Air & Space Technology Conference, Singapore, February 10-14, 1994, SAE 940041.
[59] T. Aoyama, M. Aoki, N. Kondo, S. Saito, K. Kawachi, "Effect of Blade-Tip Shape on High-Speed Rotor Noise, AIAA 96-2380, 14th AIAA Applied Aerodynamics Conference, June, 1996.
[60] S. Saito, T. Aoyama, A. Ochi, N. Kondo, A. Yamaguchi, "Impulsive Noise Calculation using Overlapped Grid Method/Kirchhoff Method", 25th European Rotorcraft Forum, Rome, September 14-16, 1999.
[61] J. Zibi, C. Polacsek, O. Rouzaud, T. Aoyama, and S. Saito, "Prediction of High-Speed Impulsive Noise Using ONERA and NAL Euler/Kirchhoff Methods, AHS International Meeting on Advanced Technology and Disaster Relief, Gifu, April 21-23, 1998.
[62] T. Aoyama, N. Kondo, M. Aoki, H. Nakamura and S. Saito, "Calculation of Rotor Blade-Vortex Interaction Noise Using Parallel Super Computer", 22nd European Rotorcraft Forum, September, 1996.
[63] A. Ochi, E. Shima, T. Aoyama, and S. Saito: Parallel Numerical Computation of Helicopter Rotor by Moving Overlapped Grid Method, AHS International Meeting on Advanced Technology and Disaster Relief, Gifu, April 21-23, 1998.
[64] H. Nakamura, H. Nishimura, N. Kondo, E. Yamakawa, T. Aoyama, and S. Saito, "Effect of Blade Geometry on BVI Noise in Various Flight Conditions, AHS International Meeting on Advanced Technology and Disaster Relief, Gifu, April 21-23, 1998.
[65] A. Ochi, E. Shima, E. Yamakawa, T. Aoyama, and S. Saito, "Aerodynamic and Aeroacoustic Analysis of BVI by Moving Overlapped Grid Method, 24th European Rotorcraft Forum, France, September 15-18, 1998.
[66] H. Nishimura, N. Kondo, H. Nakamura, T. Tsujiuchi, E, Yamakawa, T. Aoyama, and S. Saito, "Comparison between Calculated Rotor Noise and Experimental Data Obtained by DNW Test, 24th European Rotorcraft Forum, France, Marseille, September 15-18, 1998.
[67] A. Ochi, E. Shima, T. Aoyama, and S. Saito, "A Numerical Analysis of Blade-Vortex Interaction Noise using Euler CFD Code", 36th Aircraft Symposium International Session, October, 1998.
[68] T. Aoyama, A. Ochi, S. Saito and E. Shima, "Parallel Calculation of Helicopter BVI Noise by Moving Overlapped Grid Method", Parallel CFD ’99, Williamsburg, June, 1999.
[69] A. Ochi, T. Aoyama, S. Saito, E. Shima and E. Yamakawa, "BVI Noise Predictions by Moving Overlapped Grid Methods", 55th American Helicopter Society Annual Forum, Montreal, June, 1999.
[70] T. Aoyama and S. Saito, "Fundamental Study on Propagation of Blade-Vortex Interaction Noise by CFD/FW-H Method", 1st International Conference on Computational Fluid Dynamics (ICCFD), Kyoto, July, 2000.
[71] N. Kondo, A. Ochi, H. Nakamura, T. Aoyama, S. Saito and E. Yamakawa, "Validation of Rotor Aerodynamics and Aeroacoustics Prediction Methods using ATIC 2nd Model Rotor", 26th European Rotorcraft Forum, September, 2000.
[72] Y. Tanabe, S. Saito, C. Yang, T. Aoyama, A. Hashimoto and Y. Nakamura, "Aeroacoustic and Aeroelastic Simulation of HARTII Model Rotor With Moving Overlapped Grid Approach", Inter Noise 2006, December 5th 2006.
[73] Y. Tanabe, S. Saito, C. Yang, T. Aoyama, C. Benoit, J.-O. Gretay, G. Jeanfaivre, S. Peron, J. Sides, "Inviscid Numerical Simulations of 2D Parallel Blade-Vortex Interaction, JAXA/ONERA Cooperation, JAXA-RR, March 2007.
[74] Y. Tanabe, S. Saito, K. Takasaki and H. Fujita, "A parametric study on parallel Blade-Vortex-Interaction Noise", Inter Noise 2006, December 5th 2007, August 29th 2007.

[75] S. Peron, C. Benoit, T. Renaud, J. Sides Y. Tanabe, S. Saito, C. Yang and T. Aoyama, "ONERA/JAXA common investigations on CFD tools for an accurate prediction of BVI", American Helicopter Society, Korea Chapter AHS Specialists' Meeting, October 15th 2007.
[76] Y. Tanabe, S. Saito and N. Kobiki, "An Experimental Study of Rotor/Fuselage Interaction", 35th European Rotorcraft Forum, September22th 2009
[77] Y. Tanabe, S. Saito and I. Otani, "Numerical Simulations of Rotor/Fuselage Interactions Utilizing an All-Speed Scheme", 2nd International Forum on Rotorcraft Multidisciplinary Technology, October18th 2009.
[78] O. Takayama, D. Sasaki, N. Kazuhiro, Y. Tanabe and S. Saito, "Coupling Method of Unstructured and Structured Grids for Flow Around ROBIN Configuration", 2nd International Forum on Rotorcraft Multidisciplinary Technology, October18th 2009
[79] S. Saito, Y. Okuno, M. Harada, K. Funabiki and S. Akamatsu, "Feasibility Study of a Fire Fighting Helicopter for High Buildings", 20th European Rotorcraft Forum, Amsterdam, October 4-7, 1994.
[80] A. Tan, T. Kawada, A. Azuma, S. Saito and Y. Okuno, "Theoretical and Experimental Studies on System Identification of Helicopter Dynamics", 20th European Rotorcraft Forum, Amsterdam, October 4-7, 1994.

Japan Aerospace
Exploration Agency